

Kitaev Interactions Through an Extended Superexchange Pathway in the $j_{\text{eff}} = 1/2$ Ru³⁺ Honeycomb Magnet, RuP₃SiO₁₁

Aly H. Abdeldaim^{1,2*}, Hlynur Gretarsson³, Sarah J. Day⁴,
M. Duc Le², Gavin B. G. Stenning², Pascal Manuel²,
Robin S. Perry^{2,5}, Alexander A. Tsirlin⁶, Gøran J. Nilsen^{2*},
Lucy Clark^{1*}

¹School of Chemistry, University of Birmingham,
Edgbaston, Birmingham, B15 2TT, UK.

²ISIS Neutron and Muon Source, Didcot, Oxfordshire, OX11 0QX, UK.

⁴Diamond Light Source, Didcot, Oxfordshire, OX11 0DE, UK.

³Deutsches Elektronen-Synchrotron DESY, Hamburg,
D-22607, Germany.

⁵London Centre for Nanotechnology and Department of Physics and
Astronomy, University College London, London, WC1E 6BT, UK.

⁶Felix Bloch Institute for Solid-State Physics,
University of Leipzig, Leipzig, 04103, Germany.

*Corresponding author(s). E-mail(s): aly.abdeldaim@diamond.ac.uk[†];
goran.nilsen@stfc.ac.uk; l.m.clark@bham.ac.uk;

Abstract

Magnetic materials are composed of the simple building blocks of magnetic moments on a crystal lattice that interact via short-range magnetic exchange interactions. Yet from these simple building blocks emerges a remarkable diversity of magnetic states. Some of these, such as ferromagnetism, are familiar in our everyday lives, while others reveal the deep quantum mechanical origins of magnetism. A prime example of the latter are quantum spin liquid (QSL) states in which—unlike in a ferromagnet where magnetic moments are driven by their exchange interactions to adopt long-range order—magnetic moments remain disordered at low temperatures but are simultaneously correlated over long length scales through quantum entanglement. Realising such states holds significant

promise for advancing our understanding of quantum many-body physics as well as our ability to design materials for next-generation quantum technologies. A particularly promising theoretical model of a QSL is the Kitaev model, composed of unusual bond-dependent exchange interactions between magnetic moments on a honeycomb lattice. However, the Kitaev QSL is extremely challenging to realise experimentally as it is unstable to competing exchange interactions and crystal lattice perturbations that inevitably arise in real materials. This makes it essential to understand the relationship between the structure and interactions that may give rise to Kitaev interactions in new candidate materials. Here we show that the material requirements for the Kitaev QSL survive for an extended pseudo-edge-sharing superexchange pathway of $\text{Ru}^{3+} 4d^5$ octahedra within the honeycomb layers of the inorganic framework solid, $\text{RuP}_3\text{SiO}_{11}$. Through materials synthesis and structural characterisation, resonant inelastic X-ray and neutron scattering experiments, we confirm the requisite $j_{\text{eff}} = \frac{1}{2}$ state of Ru^{3+} in $\text{RuP}_3\text{SiO}_{11}$ and resolve the hierarchy of exchange interactions that provide experimental access to an otherwise unexplored region of the extended Kitaev phase diagram. This demonstrates the importance of inorganic and hybrid framework materials in the design of new Kitaev QSL candidates, as the relevant exchange interactions in their more open crystal structures may be more readily tuned than in their dense inorganic counterparts studied to date.

Keywords: Quantum materials, Kitaev quantum spin liquid, materials synthesis, neutron scattering, X-ray scattering.

†Current address: Diamond Light Source, Didcot, Oxfordshire, OX11 0DE, UK.

1 Introduction

The pursuit of new magnetic materials which allow us to explore and potentially exploit novel quantum states of matter serves as an important demonstration of the symbiosis between condensed matter experiment and theory. Traditionally, the impetus to search for novel phenomena in magnetic materials stems directly from advances in theory—a prime example being the landmark developments of the concepts of topology in condensed matter [1, 2] that are a major motivation for modern experimental materials research [3]. But increasingly, the design and synthesis of new magnetic materials provide an equally important guide to push the boundaries of state-of-the-art theory. Materials-led discoveries often highlight the critical role played by the complexities of real magnetic systems—such as further near-neighbour exchange interactions, lattice distortions and disorder—that go beyond idealised models of magnetism but ultimately govern the magnetic properties we can observe and exploit [4]. Quantum spin liquids (QSLs) present particularly compelling challenges for both experiment and theory and are highly sought by both communities for their manifestation of long-range quantum entanglement and topological excitations that may provide alternative routes to quantum computing [5]. Experimentally, QSLs are widely sought in magnetic materials where the underlying crystal structure introduces a geometric frustration that prevents the simultaneous energy minimisation of

every pair-wise magnetic exchange interaction within the system [6]. However, from a theoretical perspective, this geometric magnetic frustration often compromises the analytical and numerical tractability of the exchange Hamiltonian of model systems that are predicted to host QSL ground states, such that the true nature of the QSL states predicted for many archetypal models of geometrically frustrated magnetism is still outstanding [7, 8]. For instance, the character of the QSL describing the ground state of the $S = \frac{1}{2}$ Heisenberg kagome antiferromagnet is still widely debated [9, 10] and while several materials candidates of this model have been identified [11], the presence of disorder within their crystal structures makes it challenging to determine unambiguously the most relevant model to describe the correct magnetic ground state [12–14]. Accordingly, magnetic models with exactly solvable QSL ground states that can be extended to account for the complexities of candidate materials are highly attractive.

In this vein, the Kitaev model serves as an important and rare example of an exactly solvable model of frustrated magnetism [15]. It is most widely formulated in terms of a honeycomb lattice of ferromagnetically coupled magnetic moments (see Figure 1a), whose interactions are frustrated by an easy-axis exchange anisotropy orthogonal to the bond that connects nearest-neighbour moments [16]. The resulting exchange Hamiltonian is commonly represented in a cubic Cartesian reference frame as [8, 17]

$$\mathcal{H} = \sum_{\langle i,j \rangle \in \gamma} K_{ij}^{\gamma} S_i^{\gamma} S_j^{\gamma}, \quad (1)$$

where the summation of the spin operators, S , covers the $\langle i, j \rangle$ pairs of nearest-neighbour spins along some $[\alpha, \beta, \gamma] = [(y, x, z), (z, x, y), (x, y, z)]$ bond direction, and K is the bond-dependent Kitaev exchange interaction (see Figure 1a). In the quantum limit, the Kitaev model is exactly solvable by fractionalizing the spin degrees of freedom into Majorana fermions and gauge fluxes, yielding a QSL ground state with characteristic topological excitations [15].

Initially, it was unclear how the bond-dependent exchange interactions of the Kitaev model could be realised experimentally in a magnetic material until the breakthrough development of the Jackeli-Khaliullin mechanism, a superexchange theory that sets out the structural and electronic criteria required for the formation of dominant Kitaev-like interactions in real materials [18]. The Jackeli-Khaliullin mechanism demonstrates that the Kitaev model can be realised by placing spin-orbit entangled $j_{\text{eff}} = \frac{1}{2}$ moments on a two-dimensional honeycomb lattice via an edge-sharing octahedral connectivity. The anisotropy of this spin-orbit entangled state ensures that exchange interactions between neighbouring $j_{\text{eff}} = \frac{1}{2}$ moments are extremely sensitive to their bonding geometry, giving rise to the frustrated bond-dependent exchange interaction through a 90° metal-ligand-metal edge-sharing geometry. This arrangement ensures that the electron hopping processes responsible for the isotropic nearest-neighbour Heisenberg interaction, J , exactly cancel out, leaving only the anisotropic Kitaev interaction, K , as the dominant energy scale. While this theory

was originally developed for low-spin d^5 electronic configurations, more recent work has extended the Jackeli-Khaliullin mechanism to include d^7 [19, 20] and f -electron [21] systems with strong spin-orbit coupling.

The requirements of the Jackeli-Khaliullin mechanism, however, pose considerable synthetic challenges for realising candidate materials for the Kitaev QSL. For the originally proposed d^5 electronic configuration, only five transition metal ions with sufficiently strong spin-orbit coupling required for the requisite $j_{\text{eff}} = \frac{1}{2}$ state are available for study, with, typically, chemically inaccessible oxidation states. This is reflected in the very limited pool of candidate materials studied in the context of the Kitaev model [22], which includes only a handful of Ru^{3+} and Ir^{4+} -containing materials, with the more synthetically challenging Re^{2+} , Os^{3+} , and Rh^{4+} -based materials remaining largely unexplored [23, 24]. Additionally, the ideal octahedral crystal field environment and edge-sharing bonding geometry are often broken by the structural symmetry of real materials [16], and the extended orbital wavefunctions of their $4d$ and $5d$ transition metal ions lead to appreciable direct nearest-neighbour exchange as well as further neighbour interactions. Therefore, additional terms in the exchange Hamiltonian are generally inevitable in candidate systems, which in turn are more accurately described by an extended Kitaev model, $\mathcal{H}_{JK\Gamma\Gamma'}$. This includes an isotropic Heisenberg exchange interaction, J , an off-diagonal bond-dependent frustrated interaction, Γ , and an additional interaction that arises from trigonal distortions to the perfect octahedral symmetry in the crystal field of candidate materials, Γ' (see Methods). The vital role that these additional exchange interactions play in driving candidate Kitaev materials away from the QSL ground state is exemplified in one of the most-studied candidate systems to date, α - RuCl_3 [22, 25, 26]. Despite hosting all prerequisites for dominant Kitaev interactions, the ground state of α - RuCl_3 is magnetically ordered [27, 28]. This is likely because in addition to a dominant ferromagnetic Kitaev interaction, significant contributions from all other terms in the extended $\mathcal{H}_{JK\Gamma\Gamma'}$ model along with further-neighbour interactions are present in the exchange Hamiltonian of α - RuCl_3 [17, 29]. However, the proximity of the ground state of α - RuCl_3 to the Kitaev QSL is still intensely debated [17, 29], and it and all other candidate materials highlight the experimental challenges in attaining the criteria described by the Jackeli-Khaliullin mechanism as well as the fragility of the Kitaev QSL [22].

Given the experimental complexities associated with the existing set of Kitaev materials, recent theoretical studies highlight the importance of extending the pool of candidates to encompass framework materials with more open and extended crystal structures than the dense inorganic materials studied to date [22]. In particular, *ab initio* studies have predicted that the Jackeli-Khaliullin mechanism will still apply via an extended pseudo-edge-sharing superexchange pathway in a metal-organic framework solid [30, 31]. At the same time, this approach should also increase the typical nearest-neighbour distances within the honeycomb layers of candidate materials, thus reducing the direct orbital overlap of $4d$ and $5d$ transition metal ions that give rise to the non-Kitaev exchange interactions in the extended $\mathcal{H}_{JK\Gamma\Gamma'}$ model [16, 31]. In this

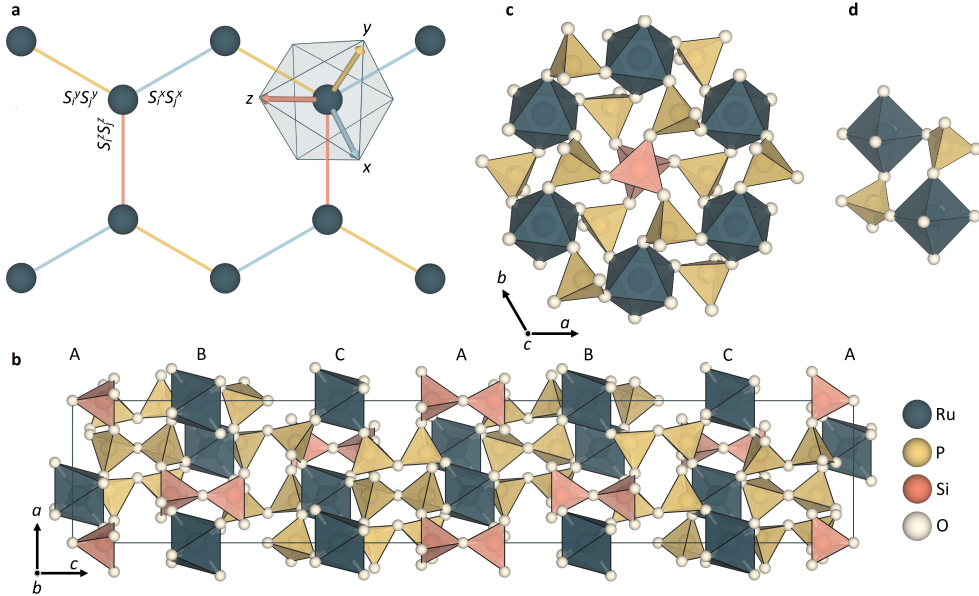


Fig. 1 Mapping the crystal structure of $\text{RuP}_3\text{SiO}_{11}$ (RPSO) to the Kitaev model on a honeycomb network. **a** The Kitaev model on a honeycomb network describes a system of magnetic moments (vertices) with anisotropic bond-dependent exchange interactions on cubic (x , y , z) axes resulting in magnetic frustration. The basis vectors of the coordinate system used to define the magnetic Hamiltonian are indicated by arrows. Such a model may be realised in materials in which $j_{\text{eff}} = \frac{1}{2}$ moments are connected on a honeycomb network via octahedral edge-sharing. **b** In the $R\bar{3}c$ crystal structure of RPSO, honeycomb layers of Ru^{3+} ions are stacked by pyrophosphate ($\text{P}_2\text{O}_7^{4-}$) and pyrosilicate ($\text{Si}_2\text{O}_7^{6-}$) units in an ABC stacking sequence along the c -axis. **c** The honeycomb rings of trigonally distorted RuO_6 octahedra viewed down the c -axis with a **d** pseudo-edge-sharing connectivity through two phosphate (PO_4^{3-}) units.

way, framework materials may provide a route to tuning the ratio of exchange interactions in the extended Kitaev model, providing experimental access to new regions of the magnetic phase diagram, including, possibly, the Kitaev QSL ground state. Motivated by this hypothesis, we have identified the inorganic framework material, $\text{RuP}_3\text{SiO}_{11}$ (RPSO), as an alternative candidate for exploring the Kitaev QSL beyond $\alpha\text{-RuCl}_3$. Through comprehensive structural characterisation and resonant inelastic X-ray scattering, we show that RPSO consists of well-separated honeycomb layers of pseudo-edge-sharing $j_{\text{eff}} = \frac{1}{2}$ Ru^{3+} ions. Magnetic susceptibility, specific heat, and neutron diffraction measurements of the low-temperature magnetic properties of RPSO confirm it adopts a magnetic ground state below $T_{\text{N}} = 1.3$ K that is distinct from $\alpha\text{-RuCl}_3$ due to its unique exchange Hamiltonian, which we show contains a dominant anisotropic Kitaev interaction through analysis of inelastic neutron scattering data. Above a critical field $H_{\text{C}} = 3.55$ T, we show that T_{N} is suppressed and RPSO enters a field-induced phase, highlighting its more readily tuneable exchange interactions in comparison to $\alpha\text{-RuCl}_3$ with $H_{\text{C}} \approx 8$ T [32].

2 Results

2.1 Crystal Structure of RPSO: Two-dimensional honeycomb layers with pseudo-edge-sharing Ru^{3+} octahedra

To determine the crystal structure of RPSO, we have performed Rietveld analysis of high-resolution synchrotron X-ray and neutron powder diffraction data. This analysis confirms that RPSO adopts a trigonal $R\bar{3}c$ structure [33] over the measured temperature range of 0.08 – 300 K (see Methods). The structure of RPSO is composed of quasi-two-dimensional buckled honeycomb layers of octahedrally coordinated Ru^{3+} ions (see Figure 1b,c). Each corner of the octahedron is occupied by an O^{2-} anion from a phosphate (PO_4^{3-}) tetrahedron. The latter connect neighbouring Ru^{3+} ions within the honeycomb layers in a pseudo-edge-sharing fashion (see Figure 1d). Each phosphate group within the honeycomb layers is part of a larger pyrophosphate ($\text{P}_2\text{O}_7^{4-}$) linker that connects the honeycomb layers along the c -axis of the crystal structure in an ABC stacking sequence. In the centre of each honeycomb ring is a pyrosilicate ($\text{Si}_2\text{O}_7^{6-}$) group which stabilises the open inorganic framework structure (see Figure 1c). The arrangement of the pyrophosphate groups within the crystal structure of RPSO results in a subtle trigonal distortion of the Ru^{3+} octahedral crystal field, with two distinct Ru-O bond lengths within each octahedron of 2.027(1) Å and 2.049(1) Å at 300 K.

Inspection of the crystal structure of RPSO allows us to infer the possible magnetic exchange pathways between neighbouring Ru^{3+} ions. The leading nearest-neighbour exchange interaction within the honeycomb layers, J , occurs through the two equivalent Ru-O-P-O-Ru pathways of the two phosphate groups generating the pseudo-edge-sharing connectivity of neighbouring octahedra (see Figure 1d). The next-nearest-neighbour exchange interaction within the honeycomb layers does not have an obvious superexchange pathway, while the further-neighbour coupling, J_3 , requires a much longer pathway comprised of one silicate and two phosphate groups. Between the honeycomb layers, an interlayer exchange pathway, J_{\perp} , runs along the pyrophosphate linkers. Compared with $\alpha\text{-RuCl}_3$, the more open framework structure extends the intra- and interlayer exchange pathways. In RPSO, the Ru-Ru distance across the nearest-neighbour exchange pathway is 4.800(1) Å compared with ≈ 3.46 Å in $\alpha\text{-RuCl}_3$ [26–28]. The interlayer Ru-Ru distance is also extended in RPSO to 7.172(1) Å from ≈ 6.01 Å in $\alpha\text{-RuCl}_3$ [26–28]. At the same time, the nearest-neighbour superexchange angles are comparable in both systems at $94.36(3)^\circ$ and $\approx 93.1^\circ$ in RPSO and $\alpha\text{-RuCl}_3$ [26–28], respectively. Thus, we hypothesise that the local coordination environment and connectivity of the Ru^{3+} ions in RPSO should preserve the requirements for anisotropic Kitaev exchange interactions, while the more open framework in comparison to $\alpha\text{-RuCl}_3$ should tune the hierarchy of exchange interactions within the extended $\mathcal{H}_{JK\Gamma\Gamma'}$ model and enhance the two-dimensionality of the honeycomb layers.

2.2 Local and Collective Magnetic Properties of RPSO:

$j_{\text{eff}} = 1/2$ Ru³⁺ moment and Néel ground state

An essential ingredient to produce the anisotropic Kitaev exchange coupling on the honeycomb network of RPSO is a $j_{\text{eff}} = \frac{1}{2}$ state for its Ru³⁺ ions. In the case of the $4d^5$ configuration of Ru³⁺, a $j_{\text{eff}} = \frac{1}{2}$ state emerges when a low-spin octahedral crystal field splitting, Δ_{O} , creates a single electron hole in the threefold degenerate t_{2g} manifold with electron spin $s = \frac{1}{2}$ and an effective orbital angular momentum $l_{\text{eff}} = -1$. The spin-orbit coupling interaction, λ , mixes these levels, creating the required $j_{\text{eff}} = \frac{1}{2}$ state (see Figure 2a). To examine the relevance of this spin-orbit entangled $j_{\text{eff}} = \frac{1}{2}$ state in RPSO, we measured its resonant inelastic X-ray scattering (RIXS) spectrum at the Ru L_3 -edge at 25 K (see Methods). The measured spectrum along with the calculated electronic transitions are shown in Figure 2b. A single sharp transition is observed below 1 eV, which bears a strong resemblance to the $j_{\text{eff}} = \frac{1}{2} \rightarrow \frac{3}{2}$ excitation of α -RuCl₃ [34], both in terms of its width—with a FWHM ≈ 150 meV—and its energy, $E \approx 250$ meV. Moreover, unlike in the related Ir⁴⁺ honeycomb compounds, (Na,Li)₂IrO₃ [35], no trigonal crystal field splitting is observed within the instrumental resolution. Taken together, this provides strong experimental evidence for the existence of a $j_{\text{eff}} = \frac{1}{2}$ state in RPSO.

Above 1 eV in the RIXS spectrum of RPSO (see Figure 2b), a series of peaks are observed originating from excitations into the e_g manifold of its octahedral crystal field. Although the overall spectral form is similar to α -RuCl₃, these excitation bands are shifted by about 250 meV higher in energy and are also noticeably sharper. The energy shift relative to α -RuCl₃ is due to the larger octahedral crystal field splitting expected for O²⁻ compared to Cl⁻, while the peak sharpness likely stems from a smaller overlap within the electron-hole continuum, *i.e.*, a larger optical gap. Additional insight can be gained by comparing the measured spectrum with full atomic multiplet calculations (see Methods). In particular, the Hund’s rule coupling, $J_{\text{H}} = 340$ meV, and crystal field splitting, $\Delta_{\text{O}} = 2.4$ eV, determined previously for α -RuCl₃ by RIXS [34] must be increased to $J_{\text{H}} = 460$ meV and $\Delta_{\text{O}} = 2.8$ eV for RPSO to capture the sharper e_g spectral features as well as their shift to higher energies. Such an increase in J_{H} can arise from a weaker screening effect in more insulating compounds, for example, as has been observed in K₂RuCl₆ [36] and RuX₃ ($X = \text{Cl, Br, I}$) [37]. Despite the differences in Δ_{O} and J_{H} , the spin-orbit coupling in RPSO, $\lambda = 130$ meV, is comparable to that reported for α -RuCl₃, $\lambda = 150$ meV [34], which highlights the significant role of spin-orbit coupling in the physics of RPSO.

Having established the relevance of the $j_{\text{eff}} = \frac{1}{2}$ state to the local magnetic properties of RPSO, we now turn to the collective magnetic properties and elucidation of its magnetic ground state. Curie-Weiss fitting the inverse magnetic susceptibility of RPSO (see Figure 3a, Methods) between 100 – 300 K yields a Weiss constant, $\theta_{\text{CW}} = -5.70(1)$ K, a Curie constant, $C = 0.33(1)$ emu K mol⁻¹, and a temperature-independent term, $\chi_0 = 2.90(1) \times 10^{-4}$ emu mol⁻¹. This implies dominant antiferromagnetic interactions between neighbouring Ru³⁺ moments in RPSO, and an effective moment $\mu_{\text{eff}} = 1.63(1)$ μ_{B} per Ru³⁺ ion consistent with the $j_{\text{eff}} = \frac{1}{2}$ state

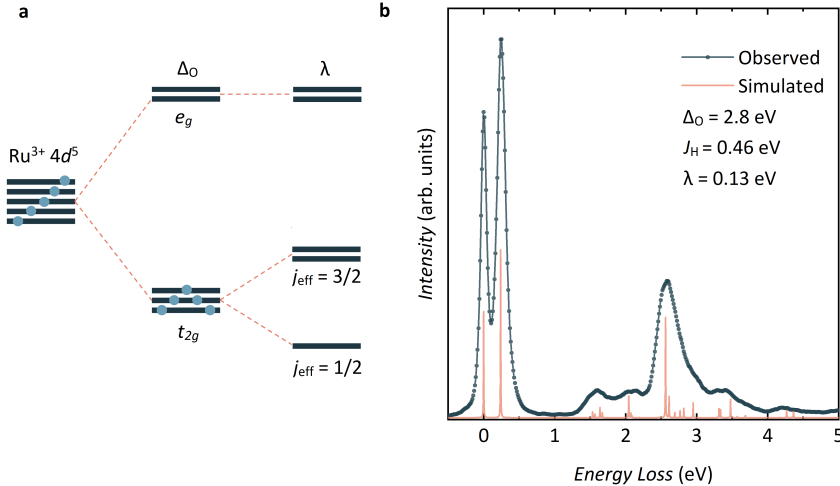


Fig. 2 Confirming the $j_{\text{eff}} = \frac{1}{2}$ state of Ru^{3+} in RPSO by resonant inelastic X-ray scattering (RIXS). **a** In an octahedral crystal field environment, the d -orbitals of a $\text{Ru}^{3+} 4d^5$ ion are split into a t_{2g} manifold with a single electron hole and an empty e_g manifold separated by the octahedral crystal field splitting parameter, Δ_O . In the presence of spin-orbit coupling, λ , the t_{2g} manifold can be further split, creating the possibility of a spin-orbit-entangled $j_{\text{eff}} = \frac{1}{2}$ moment for Ru^{3+} . If such moments are coupled by edge-sharing octahedral connectivity, then anisotropic Kitaev-type exchange interactions may dominate between them. **b** RIXS data collected for RPSO at 25 K (RIXS, DESY) confirm the $j_{\text{eff}} = \frac{1}{2}$ state of the Ru^{3+} ions in this system through the single sharp transition observed below 1 eV. The RIXS spectrum can be successfully simulated using full atomic multiplet calculations, from which estimates for the octahedral crystal field splitting, Δ_O , Hund's coupling, J_H , and spin-orbit coupling, λ , of RPSO can be extracted.

confirmed by RIXS. The temperature-independent term, χ_0 , most likely stems from the Pauli paramagnetism of the small Ru and RuO_2 phases identified in the sample by powder diffraction (see Methods). Efforts to improve the Curie-Weiss analysis by incorporating temperature-dependent magnetic moments—often a more suitable approach for strongly spin-orbit coupled systems [38]—proved inconclusive and most likely requires single-crystal magnetometry data. Below 15 K, the development of short-range magnetic correlations is evidenced in the magnetic susceptibility data through the deviation from Curie-Weiss behaviour followed by a cusp just above 1 K that indicates the onset of long-range magnetic order. This behaviour is also observed in the low-temperature specific heat data of RPSO (see Figure 3b, Methods)—where the lattice contribution to the total heat capacity will be minimal—in which a broad peak near 15 K is followed by a sharp λ -type anomaly at $T_N = 1.3$ K.

Two similar features have been observed previously in specific heat measurements of polycrystalline samples of $\alpha\text{-RuCl}_3$ [39]. These have been attributed to the onset of two magnetically ordered regimes that arise due to the presence of stacking faults between the van der Waals layers of $\alpha\text{-RuCl}_3$ [27, 39]. In the case of RPSO, the pyrophosphate and pyrosilicate linkers that pillar the honeycomb layers will increase the energy barrier to stacking fault formation compared to the weaker intermolecular

forces between the layers of α -RuCl₃, and indeed, there is no evidence of stacking faults from the peak shape and intensity of high-resolution synchrotron powder X-ray diffraction data (see Supporting Information). Alternatively, Monte-Carlo simulations have indicated that such a two-step magnetic entropy release for the extended $\mathcal{H}_{JK\Gamma\Gamma'}$ model is evidence of spin fractionalisation [40]. The temperatures at which these features appear, however, are inconsistent with the energy scales of the $\mathcal{H}_{JK\Gamma\Gamma'}$ model in RPSO obtained through analysis of inelastic neutron scattering data (see Section 2.3). Thus, we hypothesise that the broad feature near 15 K in the specific heat of RPSO simply reflects the onset of the correlated paramagnetic regime, rather than a distinct long-range ordered magnetic phase.

To determine the nature of the magnetic ground state of RPSO below $T_N = 1.3$ K, neutron magnetic scattering was isolated by subtracting neutron powder diffraction data collected above and below T_N ($\Delta T = 0.08$ K – 2.5 K, see Methods). This temperature subtraction (see Figure 3c) reveals three magnetic Bragg peaks at d -spacings corresponding to the (012), (104), and (018) reflections of the $R\bar{3}c$ crystal structure, which indicates a ground state magnetic structure described by the commensurate propagation vector, $\mathbf{k} = (0, 0, 0)$. Symmetry analysis (see Methods) results in four maximal magnetic space groups with irreducible representations that are compatible with this propagation vector and the underlying crystal structure of RPSO: $m\Gamma_{1+}$, $m\Gamma_{1-}$, $m\Gamma_{2+}$ and $m\Gamma_{2-}$ in Miller-Love notation [41]. Here, $m\Gamma_{2+}$ corresponds to a ferromagnetically ordered structure, while the $m\Gamma_{2-}$, $m\Gamma_{1+}$ and $m\Gamma_{1-}$ modes describe C, A and G-type Néel ordered states, respectively. We also considered the magnetic subgroups defined by the irreducible representations $m\Gamma_{3+}$ and $m\Gamma_{3-}$. Refining each of these models against the temperature-subtracted data reveals that only the model corresponding to the G-type Néel order ($m\Gamma_{1-}$ representation) is consistent with the observed magnetic diffraction (see Figure 3c). Thus, the magnetic ground state of RPSO is composed of antiferromagnetic honeycomb layers of Ru³⁺ ions that couple antiferromagnetically along the c -axis (G-type Néel order, see Figure 3d). The ordered magnetic moment obtained from this magnetic structure refinement, $\mu_{\text{ord}} = 0.35(1) \mu_B$ per Ru³⁺, is reduced from the full $j_{\text{eff}} = \frac{1}{2}$ ordered moment of $1 \mu_B$ and the calculated ordered moment for the $S = \frac{1}{2}$ honeycomb Heisenberg antiferromagnet with $\mu_{\text{ord}} \approx 0.55 \mu_B$ [42]. Such a reduced ordered moment is characteristic of low-dimensional magnetic materials and implies the presence of frustrated exchange interactions. It is also consistent with the observed ordered moment in α -RuCl₃, which is typically reported in the range of 0.3 – 0.7 μ_B per Ru³⁺ ion [27, 43].

The significance of the G-type Néel ordered ground state of RPSO is that it provides experimental access to an otherwise unexplored region of the magnetic phase diagram of the extended $\mathcal{H}_{JK\Gamma\Gamma'}$ Kitaev model. Indeed, all other experimental realisations of Ru³⁺ and Ir⁴⁺ honeycomb magnets studied in the context of the Kitaev QSL and that undergo a magnetic phase transition to a long-range ordered ground state adopt either zig-zag or incommensurate spin spiral magnetic structures at low temperatures [22]. This implies that RPSO has a unique hierarchy of exchange interactions within the $\mathcal{H}_{JK\Gamma\Gamma'}$ model that gives rise to its distinct magnetic ground state. The delicate

balance of competing interactions that yields the rich magnetic phase diagram for this model means that candidate materials may be tuned from one phase to another by an external perturbation, such as applied pressure or magnetic field [44]. For instance, in the case of α -RuCl₃, the zig-zig order within the magnetic ground is suppressed upon application of a critical field $H_C \approx 8$ T, which has been attributed to the formation of a field-induced quantum critical phase [32, 45, 46].

To explore the tunability of the magnetic ground state of RPSO, we have measured the field dependence of its magnetic susceptibility $\chi(T; H)$ and isothermal magnetisation $M(H; T)$ below T_N (see Methods). Upon increasing applied field strength, the cusp in the magnetic susceptibility of RPSO—that indicates the onset of the long-range Néel order—broadens and shifts lower in temperature up to an applied field of 3.5 T, above which T_N is no longer observable down to 0.5 K (see Supporting Information). Below T_N , the isothermal magnetisation increases linearly with the applied field up to 2 T, beyond which the rate of increase in magnetisation becomes steeper before reaching a critical field, $H_C = 3.55$ T. Such a field dependence of the magnetisation is typical of a field-induced phase transition, which can be more easily observed in the field derivative of the magnetisation (see Figure 4a). The resulting field-temperature phase diagram (see Figure 4b) reveals the reduction in T_N upon increasing the applied field until a critical paramagnetic phase is reached above $H_C = 3.55$ T. Understanding the nature of this field-induced phase of RPSO—whether it is a simple field-polarised or a quantum paramagnetic state—requires further investigation of single-crystal samples, but the field-temperature phase diagram is again reminiscent of α -RuCl₃, albeit with a lower critical field, which stems from the weaker exchange interactions in RPSO.

2.3 Exchange Hamiltonian of RPSO: Kitaev interactions from inelastic neutron scattering

To understand the origin of the G-type Néel ordered ground state of RPSO, we need to establish the interactions within the underlying exchange Hamiltonian (see Methods). Experimentally, this can be achieved through the analysis of the dynamical structure factor of RPSO, $S(Q, \Delta E = \hbar\omega)_{\text{exp}}$, measured by inelastic neutron scattering (INS, see Methods). Figure 5a shows the $S(Q, \Delta E = \hbar\omega)_{\text{exp}}$ measured for RPSO below T_N at $T = 0.08$ K with an incident neutron energy $E_i = 1.78$ meV. The magnetic INS spectrum is gapped, with a gap $\Delta \approx 0.1$ meV, and two clear bands of magnetic scattering intensity are observed with bandwidths $0.1 - 0.4$ meV and $0.42 - 0.82$ meV, respectively. The sharply dispersing feature in Figure 5a above 0.8 meV is the roton excitation of superfluid ⁴He arising from the He exchange gas loaded in the sample can to cool the sample (see Methods). The intensity seen at low- $|Q|$ and small- ΔE in Figure 5a is also spurious, as verified by the observation that its $|Q|$ -dependence varies with E_i . Overall, the form of the magnetic excitation spectrum of RPSO below T_N —particularly that the spectrum is gapped—indicates a strongly anisotropic exchange Hamiltonian.

To establish the relevance of $\mathcal{H}_{JK\Gamma\Gamma'}$ in RPSO, we performed a grid search using linear spin wave theory (LSWT), in which we compared $S(Q, \Delta E = \hbar\omega)_{\text{exp}}$ to solutions

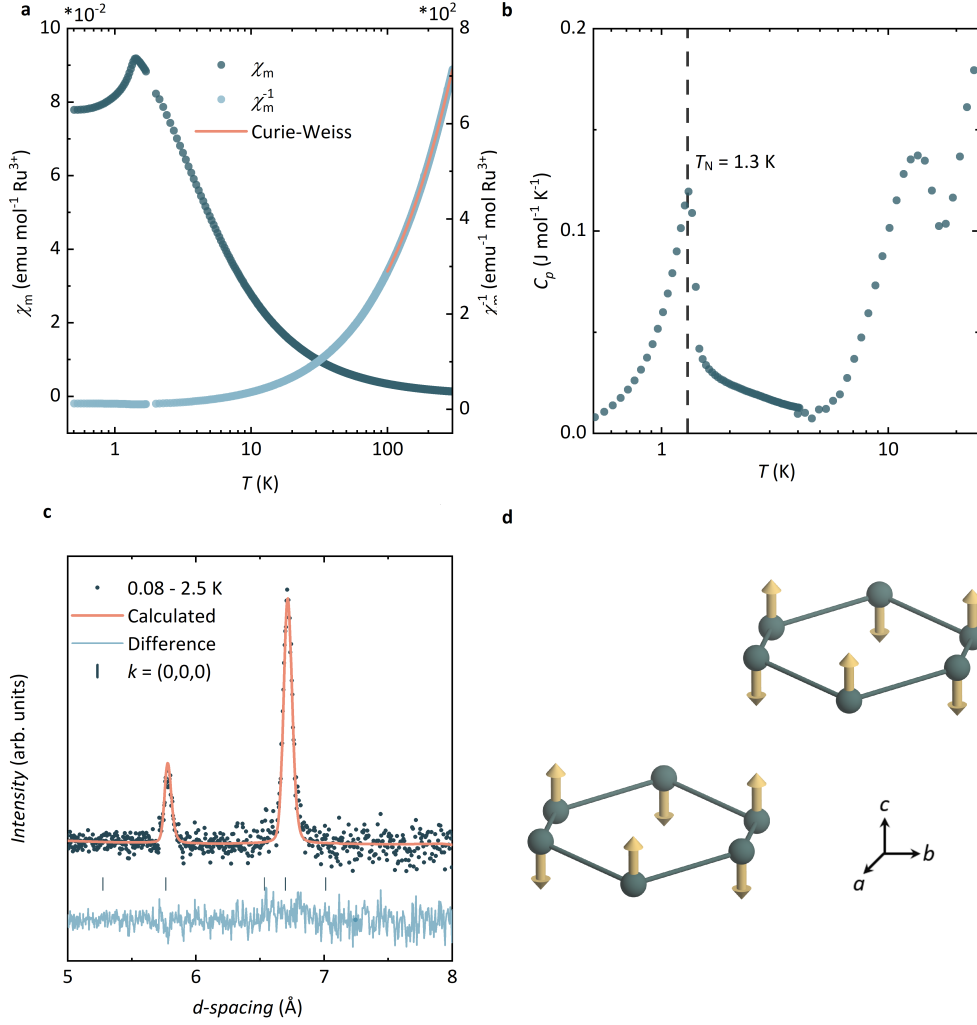


Fig. 3 Elucidating Néel order in RPSO below $T_N = 1.3$ K. **a** The magnetic susceptibility data (χ_m , left axis) measured for RPSO between 0.4 – 300 K in an applied field of 0.1 T after zero-field cooling shows a cusp just above 1 K, indicating the onset of a magnetic phase transition. Curie-Weiss fitting the inverse magnetic susceptibility (χ_m^{-1} , right axis) between 100 – 300 K gives a Weiss constant, $\theta_{CW} = -5.70(1)$ K, a Curie constant, $C = 0.33(1)$ emu K mol $^{-1}$, and a temperature-independent term, $\chi_0 = 2.90(1) \times 10^{-4}$ emu mol $^{-1}$. **b** The low-temperature zero-field specific heat (C_p) of RPSO confirms the magnetic phase transition at $T_N = 1.3$ K with a sharp λ -type anomaly at this temperature. The broader feature at $T \approx 15$ K likely reflects the development of short-range magnetic correlations. **c** Temperature-subtracted powder neutron diffraction data (WISH, ISIS) reveal magnetic Bragg peaks below T_N that can be indexed with a $\mathbf{k} = (0, 0, 0)$ propagation vector. Of the four magnetic Rietveld models compatible with this \mathbf{k} and the symmetry of the crystal structure, the best magnetic Rietveld fit (shown) is obtained with the $m\Gamma_{1-}$ irreducible representation ($\chi^2 = 1.07$ and $R_{\text{mag}} = 10.2\%$). This model corresponds to the magnetic space group $R\bar{3}'c'$ and a **d** G-type antiferromagnetic order of the Ru $^{3+}$ moments in the honeycomb layers of RPSO with an ordered moment, $\mu_{\text{ord}} = 0.35(1) \mu_B$.

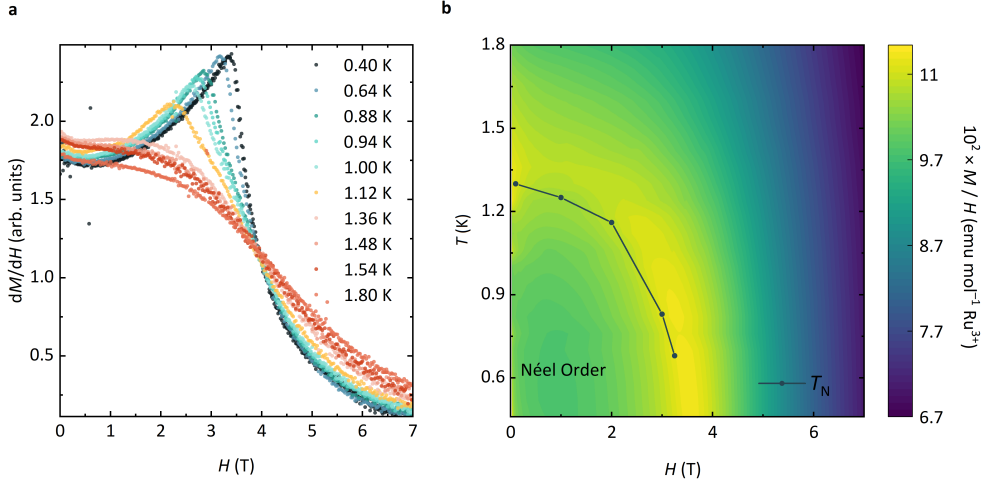


Fig. 4 Suppressing Néel order in RPSO upon application of a magnetic field. **a** The field derivative of the magnetisation isotherms shows the development of the critical field below $T_N \approx 1.3$ K. **b** The temperature-field phase diagram of RPSO mapped through magnetic susceptibility and isothermal magnetisation measurements reveals the suppression of the zero-field $T_N = 1.3$ K upon application of a magnetic field. Above a critical field of $H_C = 3.55$ T, T_N appears completely suppressed within the temperature range of the measurement.

of the extended Kitaev $\mathcal{H}_{JK\Gamma\Gamma'}$ model within the region of the phase diagram where the experimentally observed Néel ground state is stable (see Methods). The resulting sets of exchange parameters that gave the best fit to the data in the initial grid search were then further optimised using a simulated annealing algorithm (see Methods). This optimisation of the $\mathcal{H}_{JK\Gamma\Gamma'}$ model yields two regions of the phase diagram for which the fits to the experimental data are indistinguishable, which have either a dominant ferromagnetic ($K < 0$) or antiferromagnetic ($K > 0$) Kitaev exchange coupling. However, these two regions are physically equivalent and are related by the self-duality of the extended Kitaev $\mathcal{H}_{JK\Gamma\Gamma'}$ model when defined in the cubic axes of the Kitaev framework and are introduced by a global π rotation about the crystallographic c -axis (see Supporting Information) [17, 47]. Thus, we find five solutions to the $\mathcal{H}_{JK\Gamma\Gamma'}$ model that give the lowest χ^2 against the experimental data and that are well separated in χ^2 from the next set of solutions (see Table 1, Supporting Information). Figure 5b shows the $S(Q, \Delta E = \hbar\omega)_{\text{calc}}$ simulated by LSWT for the set of exchange parameters in Solution 1, and Figures 5c–f show representative comparisons of this solution to several Q -integrated cuts to the data. Within the ferromagnetic K region, all five of the lowest χ^2 LSWT solutions of the $\mathcal{H}_{JK\Gamma\Gamma'}$ model unveil two dominant anisotropic exchange interactions for RPSO: a ferromagnetic Kitaev exchange interaction K , which is approximately equal in strength to an antiferromagnetic Γ . In addition to these two bond-dependent, frustrated exchange interactions, we also find an antiferromagnetic isotropic nearest-neighbour exchange interaction, $J \approx -2/3 K$, and a ferromagnetic Γ' that is consistently smaller than the other three parameters. Notably, the latter aligns with our analysis of the RIXS spectrum and supporting

DFT calculations¹, which all show that the trigonal splitting of the octahedral crystal field in RPSO is small.

Further efforts to distinguish between the optimised parameters of Solutions 1 – 5 using experimental data did not yield a single, unique solution. When comparing the predicted critical field between the Néel ordered ground state and field-induced phase with the experimental $H_C = 3.55$ T, all solution sets consistently yield $H_{C,\text{calc}} = 3.8 - 4.1$ T. Additionally, calculating the mean-field Weiss constant [38] results in $\theta_{\text{CW}} \approx -1$ K for all solutions, which makes a direct comparison between the Curie-Weiss analysis of the magnetic susceptibility data and LSWT challenging. Thus, while the calculated $\mathcal{H}_{JK\Gamma\Gamma'}$ model successfully captures many of the prominent features in $S(Q, \Delta E = \hbar\omega)_{\text{exp}}$ (see Figure 5), the observed discrepancy with the experimental intensities may suggest further exchange interactions are required for a full microscopic description of RPSO. Indeed, the Ru-Ru bond symmetry of further near-neighbour couplings in RPSO allows for anisotropic exchange tensors, which can add up to an exchange Hamiltonian with at least 18 independent parameters that cannot be fit reasonably to the current powder-averaged INS data. On the other hand, this fitting discrepancy may also stem from the semi-classical formalism of LSWT, which underestimates both quasi-particle interactions [48, 49] and other quantum effects [50], and thus creates a bottleneck for the complete analysis of INS data of low-dimensional, frustrated quantum magnets. Multi-magnon interactions and the resulting reduction in the single magnon lifetime generally result in a characteristic broadening of spectral lines. These challenges have also been highlighted in the context of α -RuCl₃ [51]. Hence, in the case of RPSO, where the two dominant exchange interactions are strongly anisotropic—combined with the small ordered moment and quantum spin—we expect that the mismatch in fitting intensity arises from the limitations inherent to LSWT. A definitive determination of the exchange Hamiltonian, therefore, demands future developments in experiment and theory, including single-crystal inelastic neutron scattering measurements with neutron polarisation analysis and a more rigorous treatment of the resulting excitations, including magnon-interactions and other quantum effects.

2.4 Discussion and Outlook

While the energy scales of the exchange parameters determined for RPSO are at least an order of magnitude smaller than those observed in α -RuCl₃ [16, 17, 52], considering their relative magnitudes allows for a useful comparison of the two systems. Table 1 summarises a representative set of $\mathcal{H}_{JK\Gamma\Gamma'}$ parameters normalised to the ferromagnetic Kitaev exchange for α -RuCl₃ and RPSO. We note that Table 1 is not exhaustive, as the full microscopic description of α -RuCl₃ is still heavily debated with at least 20 estimates of the relevant exchange parameters (*e.g.*, see Table 1 in [17, 29]). However, overall, the absolute relative magnitudes of the $\mathcal{H}_{JK\Gamma\Gamma'}$ parameters appear consistent across both systems, with dominant K and Γ and smaller J

¹The trigonal field splitting of the t_{2g} manifold is obtained as $\Delta_0 = 0.06$ eV in density-functional-theory calculations. For full details of density-functional theory calculations, see Supporting Information.

and Γ' . Interestingly, the relative magnitudes of the nearest-neighbour Heisenberg exchange, J , are similar in both RPSO and α -RuCl₃. This is surprising given that one might expect the strength of this interaction to be relatively reduced by the more open framework structure of RPSO [31] and perhaps highlights the more complex influence of the multi-atom ligand facilitating the pseudo-edge-sharing superexchange on the relative magnitude of J . Otherwise, in the analysis of $S(Q, \Delta E = \hbar\omega)_{\text{exp}}$ for RPSO, the further-near-neighbour Heisenberg exchange interaction, J_3 , appears to be negligible, which is consistent with DFT (see Supporting Information). This is in stark contrast to α -RuCl₃ and other Kitaev-related materials where J_3 is at least $|K|/4$ [16, 17, 29, 53], and thus appears to be an important consequence of the more open framework structure of RPSO.

Collectively, the exchange parameters determined here for RPSO align with the classically calculated phase diagram of the extended $\mathcal{H}_{JK\Gamma\Gamma'}$ Kitaev model [29, 54], forming a line of solutions that closely border the predicted stripy antiferromagnetic and the experimentally observed incommensurate spin-spiral [22] magnetic ground states. To the best of our knowledge, this makes RPSO the first material realisation of the $\mathcal{H}_{JK\Gamma\Gamma'}$ model to fall within the Néel ordered region of the phase diagram and the second Ru³⁺-based material relevant to this model beyond the α -RuX₃ family ($X = \text{Cl, Br, I}$) [55]. Perhaps most importantly, RPSO also serves as an experimental proof-of-concept that anisotropic Kitaev interactions can be transmitted through a complex extended pseudo-edge-sharing superexchange pathway, corroborating the *ab initio* predictions of Yamada *et al.* [30, 31]. Consequently, this work significantly broadens the pool of materials suitable for exploring the Kitaev QSL. Coupled with other recent *ab initio* studies mapping the Kitaev model to more synthetically accessible d^7 systems [19, 20], this opens the door to an extensive experimental exploration of the $\mathcal{H}_{JK\Gamma\Gamma'}$ phase diagram in framework materials. Moving forward, it will also be important to investigate why the frustrated bond-dependent XY-type interaction, Γ , also appears to play a dominant role in the exchange Hamiltonian of a multi-atom superexchange pathway. This might be fruitful for future theoretical and experimental investigations as further framework materials are identified as candidate Kitaev systems. Nevertheless, in the case of RPSO, the extended superexchange pathway appears to have significantly diminished the influence of the further-near-neighbour Heisenberg interaction, J_3 , which is a significant energy scale in all other Kitaev-related materials studied to date [22, 29]. This—in addition to its relatively weaker exchange interactions—makes RPSO an ideal system in which to examine the effect of external perturbations, such as applied strain, pressure, and magnetic field, that may ultimately lead us to the Kitaev QSL in this inorganic framework solid.

3 Methods

3.1 Synthesis of RPSO

Polycrystalline samples of RuP₃SiO₁₁ (RPSO) were prepared via a three-step synthesis. In the first step, a precursor of RPSO, H₂RuP₃O₁₀, was synthesised via a modified

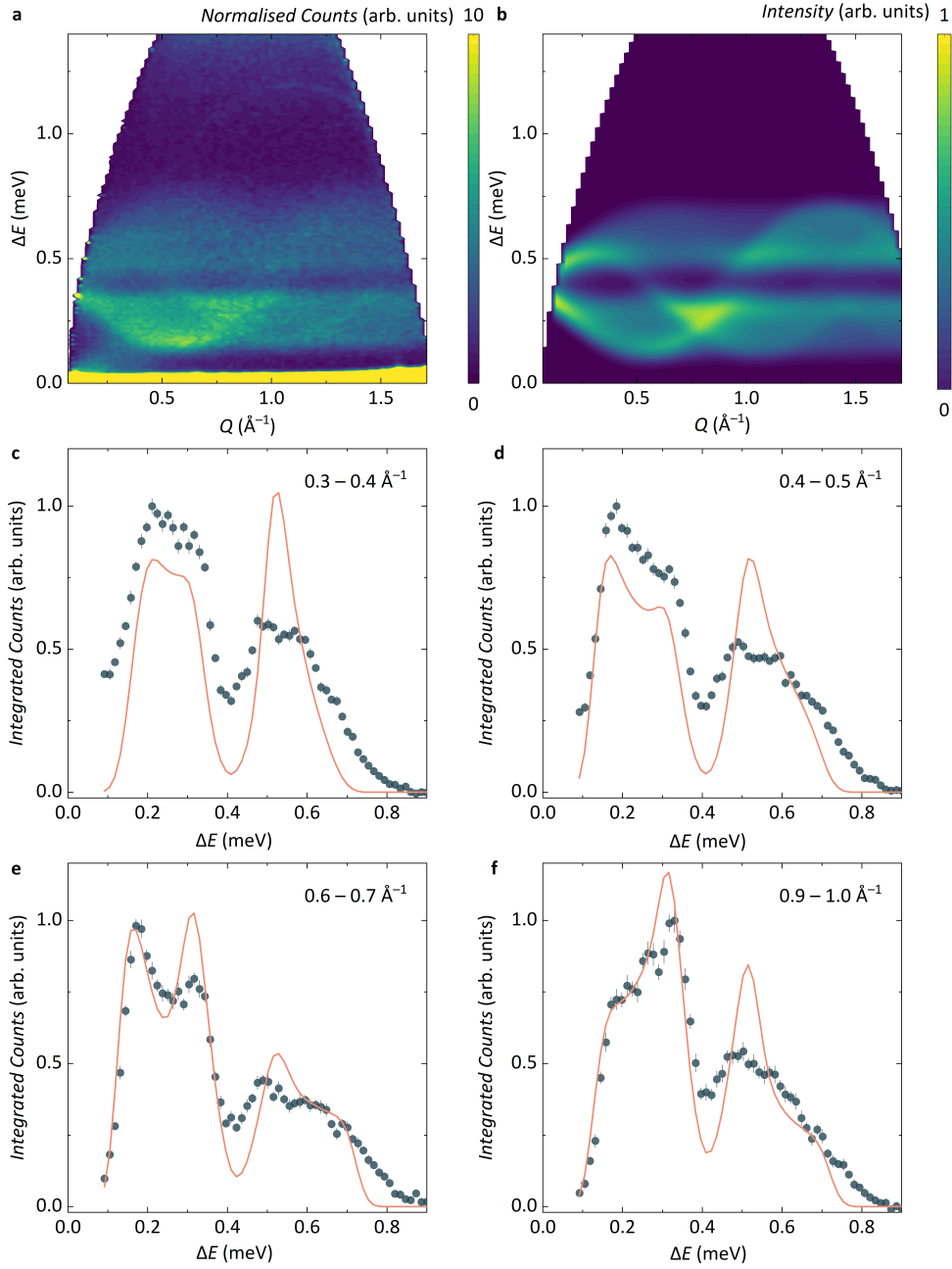


Fig. 5 Determining the exchange Hamiltonian of RPSO through inelastic neutron scattering **a** Experimental dynamical structure factor, $S(Q, \Delta E = \hbar\omega)_{\text{exp}}$, measured at 0.08 K with neutrons of incident energy $E_i = 1.78$ meV (LET, ISIS). **b** Powder-averaged and energy-convoluted $S(Q, \Delta E = \hbar\omega)_{\text{calc}}$ simulated using linear spin wave theory for the exchange Hamiltonian, $\mathcal{H}_{JK\Gamma\Gamma'}$, with $J = 0.32$ meV, $K = -0.54$ meV, $\Gamma = 0.44$ meV, and $\Gamma' = -0.12$ meV (Solution 1, Table 1). **c-f** ΔE -integrated cuts (blue circles) fitted to $S(Q, \Delta E = \hbar\omega)_{\text{calc}}$ (red lines).

Table 1 Exchange parameters (in meV) of the lowest χ^2 solutions of the $\mathcal{H}_{JK\Gamma\Gamma'}$ model obtained for RPSO in this work by fitting inelastic neutron scattering data to linear spin wave theory. For comparison, the range of $-K$ normalised exchange parameters reported for α -RuCl₃ [16, 17, 52] have also been included.

RPSO	J	K	Γ	Γ'	χ^2
Solution 1	0.32	-0.54	0.44	-0.12	67.7
Solution 2	0.23	-0.31	0.38	-0.08	68.9
Solution 3	0.16	-0.15	0.33	-0.04	69.7
Solution 4	0.25	-0.39	0.41	-0.08	69.7
Solution 5	0.37	-0.65	0.49	-0.14	70.5
Normalised	J	K	Γ	Γ'	J_3
RPSO	0.60 – 1.10	-1	0.75 – 2.20	-0.22 – -0.27	-
α -RuCl ₃ [16, 17, 52]	-0.30 – -0.53	-1	0.41 – 0.85	0.22 – 0.52	0.25 – 0.50

procedure reported in the literature [33]. In a typical reaction, RuCl₃·*x*H₂O (Sigma-Aldrich, 99.98%) and H₃PO₄ (Sigma-Aldrich, 85 wt.% in H₂O, 99.99% trace metals basis) were combined in a round bottom flask in a 1 : 4 molar ratio, respectively, and heated in air at 350 K for 6 hours under constant stirring. The resulting viscous brown solution was transported to an alumina crucible and heated at 1 K min⁻¹ to 650 K under flowing Ar gas. After 7 days of heating, the furnace was cooled to room temperature at a rate of 1 K min⁻¹. This resulted in a light brown, water insoluble, and glass-like amorphous product, which has been reported as H₂RuP₃O₁₀ [56]. In the second step, a water-washed pressed-powder pellet of H₂RuP₃O₁₀ was heated for 7 days in an evacuated sealed quartz ampoule refilled with 425 mbar of Ar gas to form a pale orange powder of Ru(PO₃)₃. Temperature control at this stage of the reaction is crucial, as Ru(PO₃)₃ can adopt three different polymorphs [56] of which the monoclinic cyclo-hexaphosphate (Ru₂P₆O₁₈)—prepared by slow heating (0.5 K min⁻¹) to 823 K—reacts to form RPSO. Finally, in the third step, a stoichiometric mixture of Ru(PO₃)₃ and SiO₂ (Alfa Aesar, 99.99%) was ground for 30 minutes, pressed into a pellet and sealed in an evacuated quartz ampoule refilled with 425 mbar of Ar gas without a crucible. This mixture was heated at 3 K min⁻¹ to 1233 K for 3 days before cooling to room temperature. The resulting final product of RPSO is yellow coloured, water insoluble and air stable for at least a month.

3.2 Crystal and Magnetic Structure Determination

High-resolution synchrotron powder X-ray diffraction data were collected on the I11 beamline at the Diamond Light Source using the MAC detector. The sample was densely packed in a 0.5 mm borosilicate capillary by sonication and diffraction data were measured at 300 K with an incident wavelength of $\lambda = 0.826015(5)$ Å. Neutron powder diffraction data were collected on the time-of-flight diffractometer WISH at the ISIS Neutron and Muon Source. 1 g of RPSO powder was packed in a cylindrical copper can and diffraction data were measured at 0.08 K and 2.5 K using a dilution

refrigerator. Crystal structure Rietveld refinements to 300 K (X-ray), 2.5 K and 0.08 K (neutron) diffraction data were performed using the GSASII [57] software package (Fig. A1, Supporting Information). For the Rietveld analysis of data collected at 300 K, lattice parameters, atomic positions and isotropic thermal parameters were varied within the $R\bar{3}c$ structural model, yielding the refined structure summarised in Table A1 (Supporting Information). Additional phases of RuO₂ and Ru metal were found to account for approximately 4.6% of the sample mass. For the Rietveld fit to 2.5 K data, lattice parameters, atomic positions and isotropic thermal parameters were varied, with additional Al and Cu phases modelled using the Le Bail method to account for the scattering from the dilution fridge insert and sample can used (Table A2), Supporting Information). At 0.08 K, all structural and instrumental parameters were fixed to their values obtained from the 2.5 K fit, with the exception of the lattice parameters, which contracted isotropically upon cooling. Representational analysis and magnetic structure refinements performed against temperature-subtracted ($\Delta T = 0.08 \text{ K} - 2.5 \text{ K}$) neutron diffraction data utilised the MAXMAGN [58] and FullProf suite [59] softwares, respectively. The Ru³⁺ form factor used was interpolated from data presented in [60].

3.3 Magnetic Susceptibility and Specific Heat Measurements

Temperature-dependent magnetic susceptibility data were measured in DC mode for a 28 mg sample of RPSO in a Quantum Design MPMS3 with a low-temperature ³He insert. Data were collected in an applied field of 0.1 T between 0.4 – 300 K in both zero-field cooled and field-cooled protocols. The sample was contained within a gelatine capsule packed tightly with Teflon tape and held in a plastic straw. Additional temperature-dependent magnetic susceptibility measurements were carried out within the temperature range of 0.4 – 1.78 K. These measurements were taken in 1 T steps of applied field between 1 – 5 T and additionally at 3.25 T, 3.5 T, 3.75 T and 4.25 T. Isothermal magnetisation data were measured over the temperature range of 0.40 – 1.8 K, with measurements taken in increments of 0.06 K, over an applied magnetic field range of $-7 - 7$ T. Specific heat data were measured on a Quantum Design Physical Property Measurement System (PPMS). 2.6 mg of RPSO was pressed into a pellet, mounted onto a puck using Apiezon N-grease and 300 data points were recorded in zero applied magnetic field between 2 – 300 K using a cryostat and between 0.1 – 4 K using a dilution refrigerator. The measurement at each temperature point was repeated twice to obtain an average.

3.4 Resonant Inelastic X-ray Scattering

Resonant inelastic X-ray scattering (RIXS) data were collected on the IRIXS instrument at beamline P01 of PETRA III synchrotron radiation source at DESY. RPSO powder was pressed into a pellet and mounted on a copper sample holder. The position of the zero-energy-loss spectral line was determined by measuring non-resonant spectra from glue deposited next to the sample. Data were collected at 25 K at the Ru L_3 -edge, where the overall energy resolution (FWHM) of the IRIXS spectrometer is

75 meV. To model the measured RIXS spectrum of RPSO, full atomic multiplet calculations were performed using the Quancy code [61] assuming a $4d^5$ configuration for Ru^{3+} . Spin-orbit coupling (λ), Hund's rule coupling (J_H), and octahedral crystal field splitting (Δ_O) were included in the model Hamiltonian for RPSO, similar to the fitting approach developed for recent measurements of $\alpha\text{-RuX}_3$ ($X = \text{Cl, Br, I}$) [37, 62]. These three parameters were then refined to best fit the experimental data.

3.5 Defining the Exchange Hamiltonian

The extended Kitaev model, $\mathcal{H}_{JK\Gamma\Gamma'}$, used widely to describe the relevant exchange Hamiltonian of candidate Kitaev materials is defined as

$$\begin{aligned} \mathcal{H}_{JK\Gamma\Gamma'} = & \sum_{\langle ij \rangle \in \gamma} [J \mathbf{S}_i \cdot \mathbf{S}_j + K S_i^\gamma S_j^\gamma + \Gamma (S_i^\alpha S_j^\beta + S_i^\beta S_j^\alpha) \\ & + \Gamma' (S_i^\alpha S_j^\gamma + S_i^\gamma S_j^\alpha) \pm \Gamma'_{ij} (S_i^\beta S_j^\gamma + S_i^\gamma S_j^\beta)] + \sum_{\langle\langle\langle ij \rangle\rangle\rangle} J_3 \mathbf{S}_i \cdot \mathbf{S}_j. \end{aligned} \quad (2)$$

Here, J is the isotropic Heisenberg exchange interaction, Γ —which is symmetry allowed in the Kitaev model—is an off-diagonal bond-dependent frustrated XY-type interaction that depends on a complex combination of metal-metal and metal-ligand assisted electron hoppings, Γ' is dependent on the local symmetry at the metal ion site and arises from trigonal distortions to the perfect octahedral symmetry in the crystal field of candidate materials [63], and J_3 is the third-nearest-neighbour Heisenberg exchange interaction. The \pm sign emphasises that the bond-dependent sign structure of Γ' varies depending on the frame of reference used to define the model [29].

The standard parameterisation of the extended Kitaev model in Eqn. 2 assumes C_2 symmetry at the Ru-Ru bond centre. In RPSO, the $\bar{1}$ point symmetry at the Ru-Ru bond centre allows for two more parameters in the exchange tensor, ξ and ζ . The resulting nearest-neighbour exchange tensor, \mathcal{J}_a^γ , of the exchange Hamiltonian is thus populated with six nonzero parameters such that

$$\begin{aligned} \mathcal{J}_a^x = & \begin{pmatrix} J + K & -\Gamma' - \zeta & -\Gamma' + \zeta \\ -\Gamma' - \zeta & J - \xi & \Gamma \\ -\Gamma' + \zeta & \Gamma & J + \xi \end{pmatrix}, \quad \mathcal{J}_a^y = \begin{pmatrix} J + \xi & -\Gamma' + \zeta & \Gamma \\ -\Gamma' + \zeta & J + K & -\Gamma' - \zeta \\ \Gamma & -\Gamma' - \zeta & J - \xi \end{pmatrix}, \\ \mathcal{J}_a^z = & \begin{pmatrix} J - \xi & \Gamma & -\Gamma' - \zeta \\ \Gamma & J + \xi & -\Gamma' + \zeta \\ -\Gamma' - \zeta & -\Gamma' + \zeta & J + K \end{pmatrix}, \end{aligned}$$

for spins that are projected on axes with γ defining the local basis vectors, given in

the crystallographic coordinates:

$$\begin{pmatrix} \mathbf{x} \\ \mathbf{y} \\ \mathbf{z} \end{pmatrix} = \begin{pmatrix} 0.224 & 0.112 & -0.029 \\ -0.112 & -0.224 & -0.029 \\ -0.112 & 0.112 & -0.029 \end{pmatrix}.$$

The exchange tensors furthermore transform with the threefold rotation axis of the $R\bar{3}c$ space group between bonds in the ab -plane, and the c -glide operation between adjacent planes

$$\mathcal{J}_b^x = \begin{pmatrix} J + K & -\Gamma' + \zeta & -\Gamma' - \zeta \\ -\Gamma' + \zeta & J + \xi & \Gamma \\ -\Gamma' - \zeta & \Gamma & J - \xi \end{pmatrix}, \quad \mathcal{J}_b^y = \begin{pmatrix} J - \xi & -\Gamma' - \zeta & \Gamma \\ -\Gamma' - \zeta & J + K & -\Gamma' + \zeta \\ \Gamma & -\Gamma' + \zeta & J + \xi \end{pmatrix},$$

$$\mathcal{J}_b^z = \begin{pmatrix} J + \xi & \Gamma & -\Gamma' + \zeta \\ \Gamma & J - \xi & -\Gamma' - \zeta \\ -\Gamma' + \zeta & -\Gamma' - \zeta & J + K \end{pmatrix}.$$

Alternatively, $\mathcal{H}_{JK\Gamma\Gamma'}$ can be rewritten in a basis aligned with the crystallographic axes [17, 44] of the $R\bar{3}c$ space group such that

$$\begin{aligned} \mathcal{H}_{XXZ} = \sum_{\langle ij \rangle} & \{ J_{ij}^{xy} (S_i^x S_j^x + S_i^y S_j^y) + J_{ij}^z S_i^z S_j^z \\ & - 2J_{i,j}^{\pm\pm} [(S_i^x S_j^x + S_i^y S_j^y) \tilde{c}_\alpha - (S_i^x S_j^y + S_i^y S_j^x) \tilde{s}_\alpha] \\ & - J_{i,j}^{z\pm} [(S_i^x S_j^z + S_i^z S_j^x) \tilde{c}_\alpha + (S_i^y S_j^z + S_i^z S_j^y) \tilde{s}_\alpha] \}. \end{aligned} \quad (3)$$

Here, $\tilde{c}_\alpha = \cos(\phi_\alpha)$, $\tilde{s}_\alpha = \sin(\phi_\alpha)$, and the phase $\phi_\alpha = [2\pi/3, -2\pi/3, 0]$ for the $[X, Y, Z]$ bonds, respectively. We emphasise that \mathcal{H}_{XXZ} and $\mathcal{H}_{JK\Gamma\Gamma'}$ are equivalent descriptions of the exchange Hamiltonian that are defined using different Cartesian bases. The $\mathcal{H}_{JK\Gamma\Gamma'}$ and \mathcal{H}_{XXZ} parameters are related by [17]

$$\begin{aligned} J^{xy} &= J + \frac{1}{3}(K - \Gamma - 2\Gamma'), \\ J^z &= J + \frac{1}{3}(K + 2\Gamma + 4\Gamma'), \\ 2J_{i,j}^{\pm\pm} &= -\frac{1}{3}(K + 2\Gamma - 2\Gamma'), \\ \sqrt{2}J_{i,j}^{z\pm} &= \frac{2}{3}(K - \Gamma + \Gamma'). \end{aligned} \quad (4)$$

3.6 Inelastic Neutron Scattering

Inelastic neutron scattering (INS) data were collected on the direct geometry time-of-flight cold neutron multi-chopper spectrometer, LET, at the ISIS Neutron and Muon

Source. 1 g of RPSO was packed and sealed with He exchange gas in an annular copper can mounted in a dilution refrigerator. Data were collected at 0.08 K, 2 K, 3 K, 4 K, 5 K, 10 K, and 15 K with incident neutron energies, $E_i = 1.78$ meV, 3.14 meV and 7 meV. The choppers were operated on high-flux mode with the resolution disk and pulse-removal disk choppers spinning at frequencies of 200 Hz and 100 Hz, respectively, yielding an elastic line resolution of approximately 0.03 meV at $E_i = 1.78$ meV.

To analyse the data, linear spin wave theory (LSWT) simulations were performed on the SpinW MATLAB package [64]. All computations were powder averaged and convoluted with the energy-dependent instrumental resolution. To extract the relevant exchange Hamiltonian of RPSO from the data, eight constant momentum transfer $|Q|$ cuts of the INS data collected at 0.08 K were used in the exchange parameter grid search, integrated over $\delta Q = 0.1$ Å, and centred about 0.25 – 0.95 Å in 0.1 Å steps. For each cut, the amplitude was fitted and a constant background term was subtracted. Given the large parameter space of the extended Kitaev model, we made the starting assumption that ζ , ξ , and any further neighbour couplings in RPSO are comparatively smaller than the four leading parameters, J , K , Γ and Γ' in the $\mathcal{H}_{JK\Gamma\Gamma'}$ model. This is justified by the relative magnitudes of the hopping integrals contributing to these parameters estimated by DFT (see Section A.3, Supporting Information) and the open framework structure of RPSO which will likely weaken couplings beyond nearest neighbours. In the initial grid search, the four exchange parameters in the $\mathcal{H}_{JK\Gamma\Gamma'}$ model were varied in 14 linearly spaced steps spanning two parameter spaces, one in which $-0.6 < J < 0.6$ meV, $-1 < K < 0$ meV, $-1 < \Gamma < 1$ meV, and $-1 < \Gamma' < 1$ meV, and another with the same J , Γ , and Γ' but with $0 < K < 1$ meV. Together these represent parameter spaces with ferromagnetic and antiferromagnetic Kitaev exchange coupling, K , respectively. This approach yielded multiple almost equivalent solutions (see Figure A7, Supporting Information) with the lowest χ^2 , all with either dominant anisotropic Kitaev-type ferromagnetic K and antiferromagnetic Γ interactions (see Table 1), or antiferromagnetic K for the symmetry-related dual set.

From this initial grid search, a series of local optimisations were performed around the lowest χ^2 solutions of the $\mathcal{H}_{JK\Gamma\Gamma'}$ model in an attempt to identify a unique set of exchange parameters for RPSO. These local optimisations were carried out on grid search solutions with $\chi^2 < 30$, and a simulated annealing algorithm was used to fit model exchange Hamiltonians to 60 ΔE cuts spanning the full experimental INS spectrum at 0.08 K. Three models were tested in this local optimisation **(1)** the $\mathcal{H}_{JK\Gamma\Gamma'}$ model, **(2)** the $\mathcal{H}_{JK\Gamma\Gamma'}$ model with the additional ξ and ζ exchange couplings allowed by the symmetry of the Ru-Ru bond centre in RPSO and **(3)** a 9-parameter model, including J , K , Γ , Γ' , ξ , ζ and the isotropic further-neighbour couplings J_2 , J_3 , and J_\perp . However, including parameters beyond the $\mathcal{H}_{JK\Gamma\Gamma'}$ model did not yield improved fits. While this does not conclusively dismiss the relevance of the additional parameters tested, it underscores the limitation of the powder-averaged datasets currently available, for which there is a risk of over-parameterising when adding further parameters beyond the $\mathcal{H}_{JK\Gamma\Gamma'}$ model. Further details and results of the INS fitting procedure can be found in Supporting Information.

Supporting information

Supporting Information contains further details of the crystal structure refinement of RPSO, field-dependent magnetic susceptibility and isothermal magnetisation measurements, supporting density-functional theory calculations and inelastic neutron scattering analysis.

Acknowledgments

This work was supported by the UKRI Science and Technology Facilities Council through the award of an ISIS Facility Development and Utilisation PhD Studentship to AHA as well as access to beamtime at the Diamond Light Source and ISIS Neutron and Muon Source. We also acknowledge DESY—a member of the Helmholtz Association HGF—for access to beamtime. Work at the University of Birmingham was supported by the UKRI Engineering and Physical Sciences Research Council grant EP/V028774/1. Work at the University of Leipzig was supported by the Deutsche Forschungsgemeinschaft (DFG, German Research Foundation) grant TRR 360 – 492547816. The authors thank Dr Matthew Coak (University of Birmingham) for providing helpful feedback on a manuscript draft.

Data availability

The data that support the findings of this study are available via the following:

- <https://syncandshare.desy.de/index.php/s/xZ2Jwrzw9mpDkxN> (IRIXS, DESY),
- <https://doi.org/10.5286/ISIS.E.RB2210080> (WISH, ISIS),
- <https://doi.org/10.5286/ISIS.E.RB2210081> (LET, ISIS).

Any requests for further data, analysis or code should be made to the corresponding authors.

Author contributions

LC and GJN conceived and supervised all aspects of the study. AHA devised and performed the synthesis of RPSO with support from RSP. AHA collected and analysed the magnetometry data. AHA collected heat capacity with support from GBGS. AHA collected and analysed synchrotron X-ray diffraction, neutron diffraction and neutron spectroscopy datasets with support from SJD, PM and GJN, respectively. AHA, MDL and GJN devised the analysis procedure for the neutron spectroscopy data. AAT performed and interpreted the density-functional theory calculations. HG performed and analysed resonant inelastic X-ray scattering measurements. AHA and LC wrote the manuscript with input from all the authors.

Competing interests

The authors declare no competing interests.

Table A1 Structural parameters of $\text{RuP}_3\text{SiO}_{11}$ obtained by Rietveld refinement of the $R\bar{3}c$ model against powder X-ray diffraction data measured at 300 K on I11 (Diamond). The resulting unit cell parameters are $a = b = 8.2410(1)$ Å and $c = 39.230(1)$ Å with goodness-of-fit parameters $\chi^2 = 3.55$ and $R_p = 8.06\%$.

Atom	Site	x	y	z	U_{iso} (Å ²)
Ru	12c	0	0	0.15854(1)	0.0057(1)
P	36f	0.3707(1)	0.0377(1)	0.11972(1)	0.0003(2)
Si	12c	0	0	0.04017(4)	0.0012(1)
O1	36f	0.0440(3)	0.1929(3)	0.05235(5)	0.0037(6)
O2	36f	0.2233(3)	0.0829(2)	0.12706(5)	0.0043(5)
O3	36f	0.1374(3)	0.2322(3)	0.18896(5)	0.0097(6)
O4	18e	0.2101(3)	0	$\frac{3}{4}$	0.0027(4)
O5	6b	0	0	0	0.0110(7)

Table A2 Structural parameters of $\text{RuP}_3\text{SiO}_{11}$ obtained by Rietveld refinement of the $R\bar{3}c$ model against powder neutron diffraction data measured at 2.5 K on WISH (ISIS). The resulting unit cell parameters are $a = b = 8.2297(5)$ Å and $c = 39.20(2)$ Å with goodness-of-fit parameters $\chi^2 = 3.23$ and $R_p = 5.97\%$.

Atom	Site	x	y	z	U_{iso} (Å ²)
Ru	12c	0	0	0.1583(2)	0.02(1)
P	36f	0.3720(8)	0.0381(8)	0.1196(1)	0.02(1)
Si	12c	0	0	0.0397 (3)	0.001(2)
O1	36f	0.0484(7)	0.2042(6)	0.0533(1)	0.02(3)
O2	36f	0.2273(7)	0.0877(7)	0.1273(1)	0.01(2)
O3	36f	0.1377(6)	0.2316(6)	0.1891(1)	0.009(3)
O4	18e	0.2080(8)	0	$\frac{3}{4}$	0.01(1)
O5	6b	0	0	0	0.02(3)

Appendix A Supporting Information

A.1 Crystal Structure Refinement

The $R\bar{3}c$ structural model of $\text{RuP}_3\text{SiO}_{11}$ was confirmed through Rietveld analysis of high-resolution synchrotron X-ray and neutron powder diffraction at temperatures of 300 K, 2.5 K, and 0.08 K (see Figure A1). The temperature-dependent analysis, detailed in Tables A1-A2, shows an isotropic contraction of the unit cell parameters that are consistent with the isotopic compounds, $\text{MoP}_3\text{SiO}_{11}$ [65] and $\text{FeP}_3\text{SiO}_{11}$ [66].

A.2 Temperature-Field Magnetic Phase Diagram

As shown in Figure A2a, the magnetization isotherm of RPSO measured at 0.4 K, (below $T_N = 1.3$ K), exhibits an anomaly at a critical field of $H_C = 3.55$ T. The temperature dependence of this anomaly is displayed in Figure A2b, which softens as the paramagnetic regime is approached. A closer examination of the field and temperature dependence, shown in Figure A2c, of M/H reveals that beyond 0.1 T, the anomaly indicating the onset of long-range magnetic order broadens, and its temperature dependence decreases steadily with increasing applied field. Upon reaching 3.5 T, T_N is no longer discernible within the 0.5 – 1.7 K temperature range of the measurement.

A.3 First-Principles Calculations

Ab initio methods were used to independently verify the validity of the $j_{\text{eff}} = \frac{1}{2}$ character of Ru^{3+} in RPSO as determined in the main manuscript by RIXS, as well as to investigate the nature of the exchange Hamiltonian. Density-functional theory (DFT) band structure calculations were performed in the FPLO [67] and VASP [68, 69] codes using the experimentally determined crystal structure and the Perdew-Burke-Ernzerhof (PBE) [70] flavour of the exchange-correlation potential. Correlation effects in the Ru 4d shell were accounted for on the mean-field DFT+U level with the on-site Coulomb repulsion $U = 3$ eV and Hund’s coupling $J_H = 0.46$ eV, the latter value determined by RIXS.

To validate the experimental observation of the $j_{\text{eff}} = \frac{1}{2}$ state of Ru^{3+} in RPSO and to directly compare it with $\alpha\text{-RuCl}_3$, we have performed electronic band structure calculations for both systems at the scalar relativistic level (see Figure A3). To ensure the validity of this comparison, we employed the widely accepted low-temperature rhombohedral structure for band-structure calculations of $\alpha\text{-RuCl}_3$ [71]. In this $R\bar{3}$ structure, the octahedral crystal field is trigonally distorted as in RPSO, yielding the same local 3-fold rotational symmetry at the Ru^{3+} sites of each system. Calculating the density of states allows the orbital energies of each system to be determined from their Wannier projections, and the corresponding octahedral crystal field splitting, Δ_O , for RPSO was calculated to be 2.52 eV, compared with 2.42 eV for $\alpha\text{-RuCl}_3$. The increased Δ_O for the oxide crystal field of RPSO compared with the chloride crystal field of $\alpha\text{-RuCl}_3$ is in keeping with the RIXS data analysis and reflects the greater ionic character of O^{2-} versus Cl^- . The trigonal crystal field splitting, on the other hand, is equivalent in magnitude but opposite in sign in both systems with $|\Delta_t| = 0.06$ eV. Overall, the calculated orbital energies indicate that RPSO meets the same prerequisite requirements for the formation of the $j_{\text{eff}} = \frac{1}{2}$ state for Ru^{3+} as in $\alpha\text{-RuCl}_3$, which is fully consistent with the RIXS data analysis in the main manuscript.

This conclusion is verified by calculating the PBE+SO density of states of RPSO. The resulting density of states reveals a clear splitting of the t_{2g} band into lower and higher lying $j_{\text{eff}} = \frac{1}{2}$ and $j_{\text{eff}} = \frac{3}{2}$ manifolds, respectively, as has also been seen in the PBE+SO density of states of Ir^{4+} compounds [72]. Spin-polarised calculations (PBE+U+SO) further reveal that the magnetic moments of Ru^{3+} comprise

$\mu_{\text{spin}}^x = 0.19 \mu_{\text{B}}$ of the spin contribution and $\mu_{\text{orb}}^x = 0.38 \mu_{\text{B}}$ of the orbital contribution when directed along a . Similarly, along the c axis, the magnetic moments are $\mu_{\text{spin}}^z = 0.20 \mu_{\text{B}}$ and $\mu_{\text{orb}}^z = 0.47 \mu_{\text{B}}$. The almost isotropic nature of the moment and the nearly 1 : 2 ratio of μ_{spin} and μ_{orb} are both consistent with a $j_{\text{eff}} = \frac{1}{2}$ state in RPSO.

We also expanded our DFT calculations to include the magnetic exchange interactions between the $j_{\text{eff}} = \frac{1}{2}$ states of the Ru^{3+} ions in RPSO by analysing the hopping integrals t within superexchange theory [63, 73]. Using $U = 3$ eV, as well as $J_{\text{H}} = 0.46$ eV and $\lambda = 0.13$ eV from RIXS, we find $(J, K, \Gamma, \Gamma') = (-0.16, -0.65, 0.26, -0.42)$ meV along with $\zeta = 0.03$ meV and $\xi = 0.02$ meV. These K and Γ values are compatible with the LSWT estimates, whereas Γ' seems overestimated, and J is weakly ferromagnetic, in contrast to the weakly antiferromagnetic J required for stabilising the Néel order. These discrepancies may be caused by the overall weakness of the exchange couplings and by the residual trigonal crystal-field splitting, which was not taken into account within the superexchange theory. Nevertheless, these estimates support our description of RPSO in terms of the $\mathcal{H}_{JK\Gamma\Gamma'}$ model and justify the neglect of ζ and ξ as minor terms in the spin Hamiltonian. We also estimated the interlayer coupling of $J_{\perp} = 0.18$ meV, which is somewhat weaker than the leading in-plane terms. Finally, our calculations confirm that further-neighbor in-plane couplings should be as small as $J_2 \approx 0.003$ meV and $J_3 \approx 0.0006$ meV and thus truly negligible in this material.

A.4 Inelastic Neutron Scattering Data Analysis

As shown in Figure A4, at an incident energy of $E_i = 3.14$ meV, the experimental dynamical structure factor shows only magnetic scattering. Above T_{N} , the $\Delta = 0.1$ meV gap closes, and the spectra are peaked at low $|Q|$ and show scattering up to $\Delta E \approx 0.8$ meV. This behavior is observed up to 15 K and is shown in Figure A4, which includes the spectrum and representative cuts at selected temperatures.

As detailed in the main manuscript, a grid search was used to explore and compare the $\mathcal{H}_{JK\Gamma\Gamma'}$ parameter space to the experimental dynamical structure factor at 0.08 K. The resulting five-dimensional space, encompassing the fitted parameter sets of (J, K, Γ, Γ') and their corresponding goodness-of-fit χ^2 to the data, is shown in Figures A5 and A6 for $K > 0$ and $K < 0$, respectively. Here, missing spaces in the four-dimensional spaces are solutions that are incompatible with the magnetic structure. A summary of the number of the lowest χ^2 parameter sets — subsequently used for the simulated annealing optimisation (see Methods) — is presented in Figure A7. The best fitting optimised solutions for $K < 0$ are presented in Table 1. We note that the mismatch in χ^2 values between the grid search and the simulated annealing optimisation stems from the different number of cuts used for fitting — 8 in the former and 60 in the latter.

For low χ^2 solutions with $K > 0$, we find a connection to the optimised $K < 0$ parameter sets through the self-duality of the $\mathcal{H}_{JK\Gamma\Gamma'}$ model when defined using the set of rotated cubic axes. Within this frame of reference, a physically identical set of

parameters can be obtained by applying a π rotation to the honeycomb plane about the crystallographic c -axis [17]

$$\begin{pmatrix} J \\ K \\ \Gamma \\ \Gamma' \end{pmatrix}_{\text{dual}} = \begin{pmatrix} 1 & \frac{4}{9} & -\frac{4}{9} & \frac{4}{9} \\ 0 & -\frac{1}{3} & \frac{4}{3} & -\frac{4}{3} \\ 0 & \frac{4}{9} & \frac{5}{9} & \frac{4}{9} \\ 0 & -\frac{2}{9} & \frac{2}{9} & \frac{7}{9} \end{pmatrix} \begin{pmatrix} J \\ K \\ \Gamma \\ \Gamma' \end{pmatrix}.$$

This transformation is evident for the representative optimised (J, K, Γ, Γ') parameter sets, $(-0.16, 0.86, -0.01, 0.12)$ meV and $(-0.11, 0.56, 0.12, 0.09)$ meV, with $\chi^2 = 68.8$ and 72.4 respectively. Applying the transformation matrix to these solutions yields $(0.28, -0.46, 0.43, -0.1)_{\text{dual}}$ meV and $(0.12, -0.15, 0.36, -0.02)_{\text{dual}}$ meV, corresponding approximately to Solutions 1 and 3 in Table 1.

Table A3 Exchange parameters (in meV) of the five lowest χ^2 solutions of the \mathcal{H}_{XXZ} model obtained for RPSO in this work by fitting inelastic neutron scattering data to linear spin wave theory.

RPSO	J^{xy}	J^z	$J^{\pm\pm}$	$J^{z\pm}$	χ^2
Solution 1	0.08	0.28	-0.10	-0.52	67.7
Solution 2	0.05	0.28	-0.10	-0.36	68.9
Solution 3	0.02	0.28	-0.10	-0.25	69.7
Solution 4	0.07	0.27	-0.10	-0.42	69.7
Solution 5	0.08	0.29	-0.10	-0.61	70.5

A recent trend in the literature is a growing preference for the crystallographic frame to formulate the exchange Hamiltonian of the extended Kitaev model [17, 74]. In this framework, the exchange Hamiltonian is expressed as \mathcal{H}_{XXZ} (Equation 3), and the optimised solutions in Table 1 can be rewritten using Equations 4, resulting in the parameters presented in Table A3. Using this notation, only $J^{z\pm}$ varies across the the optimised solutions, while $(J^{xy}, J^z, J^{\pm\pm})$ are consistently around $(0.05, 0.28, -0.1)$ meV.

References

- [1] Haldane, F.D.M.: Nonlinear field theory of large-spin Heisenberg antiferromagnets: Semiclassically quantized solitons of the one-dimensional easy-axis Néel state. *Phys. Rev. Lett.* **50**, 1153–1156 (1983)
- [2] Kosterlitz, J.M., Thouless, D.J.: Ordering, metastability and phase transitions in two-dimensional systems. *J. Phys. C* **6**, 1181–1203 (1973)

- [3] Bernevig, B.A., Felser, C., Beidenkopf, H.: Progress and prospects in magnetic topological materials. *Nature* **603**, 41–51 (2022)
- [4] Balz, C., Lake, B., Reuther, J., Luetkens, H., Schönemann, R., Herrmannsdörfer, T., Singh, Y., Nazmul Islam, A.T.M., Wheeler, E.M., Rodriguez-Rivera, J.A., Guidi, T., Simeoni, G.G., Baines, C., Ryll, H.: Physical realization of a quantum spin liquid based on a complex frustration mechanism. *Nat. Phys.* **12**, 942–949 (2016)
- [5] Broholm, C., Cava, R.J., Kivelson, S.A., Nocera, D.G., Norman, M.R., Senthil, T.: Quantum spin liquids. *Science* **367**, 0668 (2020)
- [6] Clark, L., Abdeldaim, A.H.: Quantum spin liquids from a materials perspective. *Annu. Rev. Mater. Sci.* **51**, 495–519 (2021)
- [7] Savary, L., Balents, L.: Quantum spin liquids: A review. *Rep. Prog. Phys.* **80**, 016502 (2016)
- [8] Hermanns, M., Kimchi, I., Knolle, J.: Physics of the Kitaev model: Fractionalization, dynamic correlations, and material connections. *Annu. Rev. Condens. Matter Phys.* **9**, 17–33 (2018)
- [9] Ran, Y., Hermele, M., Lee, P.A., Wen, X.-G.: Projected-wave-function study of the spin-1/2 Heisenberg model on the kagomé lattice. *Phys. Rev. Lett.* **98**, 117205 (2007)
- [10] Yan, S., Huse, D.A., White, S.R.: Spin-liquid ground state of the $S = 1/2$ kagome Heisenberg antiferromagnet. *Science* **332**, 1173–1176 (2011)
- [11] Norman, M.R.: Colloquium: Herbertsmithite and the search for the quantum spin liquid. *Rev. Mod. Phys.* **88**, 041002 (2016)
- [12] Han, T.-H., Helton, J.S., Chu, S., Nocera, D.G., Rodriguez-Rivera, J.A., Broholm, C., Lee, Y.S.: Fractionalized excitations in the spin-liquid state of a kagome-lattice antiferromagnet. *Nature* **492**, 406–410 (2012)
- [13] Fu, M., Imai, T., Han, T.-H., Lee, Y.S.: Evidence for a gapped spin-liquid ground state in a kagome Heisenberg antiferromagnet. *Science* **350**, 655–658 (2015)
- [14] Khuntia, P., Velazquez, M., Barthélemy, Q., Bert, F., Kermarrec, E., Legros, A., Bernu, B., Messio, L., Zorko, A., Mendels, P.: Gapless ground state in the archetypal quantum kagome antiferromagnet $\text{ZnCu}_3(\text{OH})_6\text{Cl}_2$. *Nat. Phys.* **16**(4), 469–474 (2020)
- [15] Kitaev, A.: Anyons in an exactly solved model and beyond. *Ann. Phys.* **321**, 2–111 (2006)
- [16] Winter, S.M., Tsirlin, A.A., Daghofer, M., Brink, J., Singh, Y., Gegenwart, P.,

- Valentí, R.: Models and materials for generalized Kitaev magnetism. *J. Phys. Condens. Matter.* **29**, 493002 (2017)
- [17] Maksimov, P.A., Chernyshev, A.L.: Rethinking α -RuCl₃. *Phys. Rev. Res.* **2**, 033011 (2020)
- [18] Jackeli, G., Khaliullin, G.: Mott insulators in the strong spin-orbit coupling limit: From Heisenberg to a quantum compass and Kitaev models. *Phys. Rev. Lett.* **102**, 017205 (2009)
- [19] Stavropoulos, P.P., Pereira, D., Kee, H.-Y.: Microscopic mechanism for a higher-spin Kitaev model. *Phys. Rev. Lett.* **123**, 037203 (2019)
- [20] Liu, H., Khaliullin, G.: Pseudospin exchange interactions in d^7 cobalt compounds: Possible realization of the Kitaev model. *Phys. Rev. B* **97**, 014407 (2018)
- [21] Motome, Y., Sano, R., Jang, S., Sugita, Y., Kato, Y.: Materials design of Kitaev spin liquids beyond the Jackeli–Khaliullin mechanism. *J. Phys. Condens. Matter.* **32**, 404001 (2020)
- [22] Takagi, H., Takayama, T., Jackeli, G., Khaliullin, G., Nagler, S.E.: Concept and realization of Kitaev quantum spin liquids. *Nat. Rev. Phys.* **1**, 264–280 (2019)
- [23] Kataoka, K., Hirai, D., Yajima, T., Nishio-Hamane, D., Ishii, R., Choi, K.-Y., Wulferding, D., Lemmens, P., Kittaka, S., Sakakibara, T., Ishikawa, H., Matsuo, A., Kindo, K., Hiroi, Z.: Kitaev spin liquid candidate Os_xCl₃ comprised of honeycomb nano-domains. *J. Phys. Soc. Japan* **89**, 114709 (2020)
- [24] Katukuri, V.M., Nishimoto, S., Rousochatzakis, I., Stoll, H., Brink, J., Hozoi, L.: Strong magnetic frustration and anti-site disorder causing spin-glass behavior in honeycomb Li₂RhO₃. *Sci. Rep.* **5**, 14718 (2015)
- [25] Plumb, K.W., Clancy, J.P., Sandilands, L.J., Shankar, V.V., Hu, Y.F., Burch, K.S., Kee, H.-Y., Kim, Y.-J.: α -RuCl₃: A spin-orbit assisted Mott insulator on a honeycomb lattice. *Phys. Rev. B* **90**, 041112 (2014)
- [26] Banerjee, A., Bridges, C.A., Yan, J.-Q., Aczel, A.A., Li, L., Stone, M.B., Granroth, G.E., Lumsden, M.D., Yiu, Y., Knolle, J., Bhattacharjee, S., Kovrizhin, D.L., Moessner, R., Tennant, D.A., Mandrus, D.G., Nagler, S.E.: Proximate Kitaev quantum spin liquid behaviour in a honeycomb magnet. *Nat. Mater.* **15**, 733–740 (2016)
- [27] Johnson, R.D., Williams, S.C., Haghighirad, A.A., Singleton, J., Zapf, V., Manuel, P., Mazin, I.I., Li, Y., Jeschke, H.O., Valentí, R., Coldea, R.: Monoclinic crystal structure of α -RuCl₃ and the zigzag antiferromagnetic ground state. *Phys. Rev. B* **92**, 235119 (2015)

- [28] Sears, J.A., Songvilay, M., Plumb, K.W., Clancy, J.P., Qiu, Y., Zhao, Y., Parshall, D., Kim, Y.-J.: Magnetic order in α -RuCl₃: A honeycomb-lattice quantum magnet with strong spin-orbit coupling. *Phys. Rev. B* **91**, 144420 (2015)
- [29] Rousochatzakis, I., Perkins, N., Luo, Q., Kee, H.-Y.: Beyond Kitaev physics in strong spin-orbit coupled magnets. *Rep. Prog. Phys.* (2024)
- [30] Yamada, M.G., Dwivedi, V., Hermanns, M.: Crystalline Kitaev spin liquids. *Phys. Rev. B* **96**, 155107 (2017)
- [31] Yamada, M.G., Fujita, H., Oshikawa, M.: Designing Kitaev spin liquids in metal-organic frameworks. *Phys. Rev. Lett.* **119**, 057202 (2017)
- [32] Banerjee, A., Lampen-Kelley, P., Knolle, J., Balz, C., Aczel, A.A., Winn, B., Liu, Y., Pajerowski, D., Yan, J., Bridges, C.A., Savici, A.T., Chakoumakos, B.C., Lumsden, M.D., Tennant, D.A., Moessner, R., Mandrus, D.G., Nagler, S.E.: Excitations in the field-induced quantum spin liquid state of α -RuCl₃. *npj Quantum Mater.* **3**, 8 (2018)
- [33] Fukuoka, H., Imoto, H., Saito, T.: Synthesis and crystal structure of a new ruthenium silicophosphate: RuP₃SiO₁₁. *J. Solid State Chem.* **121**, 247–250 (1996)
- [34] Suzuki, H., Liu, H., Bertinshaw, J., Ueda, K., Kim, H., Laha, S., Weber, D., Yang, Z., Wang, L., Takahashi, H., Fürsich, K., Minola, M., Lotsch, B.V., Kim, B.J., Yavaş, H., Daghofer, M., Chaloupka, J., Khaliullin, G., Gretarsson, H., Keimer, B.: Proximate ferromagnetic state in the Kitaev model material α -RuCl₃. *Nat. Commun.* **12**, 4512 (2021)
- [35] Gretarsson, H., Clancy, J.P., Liu, X., Hill, J.P., Bozin, E., Singh, Y., Manni, S., Gegenwart, P., Kim, J., Said, A.H., Casa, D., Gog, T., Upton, M.H., Kim, H.-S., Yu, J., Katukuri, V.M., Hozoi, L., Brink, J., Kim, Y.-J.: Crystal-field splitting and correlation effect on the electronic structure of A₂IrO₃. *Phys. Rev. Lett.* **110**, 076402 (2013)
- [36] Takahashi, H., Suzuki, H., Bertinshaw, J., Bette, S., Müuhle, C., Nuss, J., Dinnebier, R., Yaresko, A., Khaliullin, G., Gretarsson, H., Takayama, T., Takagi, H., Keimer, B.: Nonmagnetic $J = 0$ state and spin-orbit excitations in K₂RuCl₆. *Phys. Rev. Lett.* **127**, 227201 (2021)
- [37] Gretarsson, H., Fujihara, H., Sato, F., Gotou, H., Imai, Y., Ohgushi, K., Keimer, B., Suzuki, H.: $J = 1/2$ Pseudospins and d - p Hybridization in the Kitaev Spin Liquid Candidates RuX₃ ($X = \text{Cl, Br, I}$) (2024)
- [38] Li, Y., Winter, S.M., Kaib, D.A.S., Riedl, K., Valentí, R.: Modified Curie-Weiss law for j_{eff} magnets. *Phys. Rev. B* **103**, 220408 (2021)

- [39] Kim, S., Yuan, B., Kim, Y.-J.: α -RuCl₃ and other Kitaev materials. *APL Mater.* **10**, 080903 (2022)
- [40] Hickey, C., Trebst, S.: Emergence of a field-driven U(1) spin liquid in the Kitaev honeycomb model. *Nat. Commun.* **10**, 530 (2019)
- [41] Miller, S.C., Love, W.F.: *Tables of Irreducible Representations of Space Groups and Co-representations of Magnetic Space Groups*. Pruett Press, Colorado (1967)
- [42] Reger, J.D., Riera, J.A., Young, A.P.: Monte carlo simulations of the spin-1/2 Heisenberg antiferromagnet in two dimensions. *J. Phys. Condens. Matter.* **1**, 1855–1865 (1989)
- [43] Cao, H.B., Banerjee, A., Yan, J.-Q., Bridges, C.A., Lumsden, M.D., Mandrus, D.G., Tennant, D.A., Chakoumakos, B.C., Nagler, S.E.: Low-temperature crystal and magnetic structure of α -RuCl₃. *Phys. Rev. B* **93**, 134423 (2016)
- [44] Trebst, S., Hickey, C.: Kitaev materials. *Phys. Rep.* **950**, 1–37 (2022)
- [45] Baek, S.-H., Do, S.-H., Choi, K.-Y., Kwon, Y.S., Wolter, A.U.B., Nishimoto, S., Brink, J., Büchner, B.: Evidence for a field-induced quantum spin liquid in α -RuCl₃. *Phys. Rev. Lett.* **119**, 037201 (2017)
- [46] Hentrich, R., Hong, X., Gillig, M., Cagliaris, F., Čulo, M., Shahrokhvand, M., Zeitler, U., Roslova, M., Isaeva, A., Doert, T., Janssen, L., Vojta, M., Büchner, B., Hess, C.: High-field thermal transport properties of the Kitaev quantum magnet α -RuCl₃: Evidence for low-energy excitations beyond the critical field. *Phys. Rev. B* **102**, 235155 (2020)
- [47] Chaloupka, J., Khaliullin, G.: Hidden symmetries of the extended Kitaev-Heisenberg model: Implications for the honeycomb-lattice iridates $A_2\text{IrO}_3$. *Phys. Rev. B* **92**, 024413 (2015)
- [48] Bai, X., Zhang, S.-S., Zhang, H., Dun, Z., Phelan, W.A., Garlea, V.O., Mourigal, M., Batista, C.D.: Instabilities of heavy magnons in an anisotropic magnet. *Nat. Commun.* **14**, 4199 (2023)
- [49] Kim, C., Kim, S., Park, P., Kim, T., Jeong, J., Ohira-Kawamura, S., Murai, N., Nakajima, K., Chernyshev, A.L., Mourigal, M., Kim, S.-J., Park, J.-G.: Bond-dependent anisotropy and magnon decay in cobalt-based Kitaev triangular antiferromagnet. *Nat. Phys.* **19**, 1624–1629 (2023)
- [50] Taylor, J.H., Müller, G.: Limitations of spin-wave theory in $T = 0$ spin dynamics. *Phys. Rev. B* **28**, 1529–1533 (1983)
- [51] Winter, S.M., Riedl, K., Maksimov, P.A., Chernyshev, A.L., Honecker, A., Valentí, R.: Breakdown of magnons in a strongly spin-orbital coupled magnet.

Nat. Commun. **8**, 1152 (2017)

- [52] Liu, H., Chaloupka, J., Khaliullin, G.: Exchange interactions in d^5 Kitaev materials: From Na_2IrO_3 to $\alpha\text{-RuCl}_3$. Phys. Rev. B **105**, 214411 (2022)
- [53] Kim, J., Chaloupka, J., Singh, Y., Kim, J.W., Kim, B.J., Casa, D., Said, A., Huang, X., Gog, T.: Dynamic spin correlations in the honeycomb lattice Na_2IrO_3 measured by resonant inelastic X-ray scattering. Phys. Rev. X **10**, 021034 (2020)
- [54] Rau, J.G., Kee, H.-Y.: Trigonal distortion in the honeycomb iridates: Proximity of zigzag and spiral phases in Na_2IrO_3 (2014)
- [55] Kaib, D.A.S., Riedl, K., Razpopov, A., Li, Y., Backes, S., Mazin, I.I., Valentí, R.: Electronic and magnetic properties of the RuX_3 ($X = \text{Cl, Br, I}$) family: two siblings—and a cousin? npj Quantum Materials **7**(1), 75 (2022)
- [56] Fukuoka, H., Imoto, H., Saito, T.: New polymorphs of RuIIP_3O_9 : Cyclohexaphosphate $\text{Ru}_2\text{P}_6\text{O}_{18}$ and metaphosphate $\text{Ru}(\text{PO}_3)_3$ with a novel structure. J. Solid State Chem. **119**, 107–114 (1995)
- [57] Toby, B.H., Von Dreele, R.B.: *GSAS-II*: The Genesis of a Modern Open-source All Purpose Crystallography Software Package. J. Appl. Crystallogr. **46**, 544–549 (2013)
- [58] Perez-Mato, J.M., Gallego, S.V., Tasci, E.S., Elcoro, L., Flor, G., Aroyo, M.I.: Symmetry-based computational tools for magnetic crystallography. Annu. Rev. Mater. Res. **45**, 217–248 (2015)
- [59] Rodríguez-Carvajal, J.: Recent advances in magnetic structure determination by neutron powder diffraction. Phys. B: Condens. Matter. **192**, 55–69 (1993)
- [60] Cromer, D.T., Waber, J.T.: Scattering factors computed from relativistic Dirac–Slater wave functions. Acta Crystallogr. **18**, 104–109 (1965)
- [61] Haverkort, M.W.: Quanta for core level spectroscopy - excitons, resonances and band excitations in time and frequency domain. J. Phys. Conf. Ser. **712**, 012001 (2016)
- [62] Yang, Z., Wang, L., Zhao, D., Luo, M., Laha, S., Güth, A., Taniguchi, T., Watanabe, K., Lotsch, B.V., Smet, J.H., Minola, M., Gretarsson, H., Keimer, B.: Resonant inelastic x-ray scattering from electronic excitations in $\alpha\text{-RuCl}_3$ nanolayers. Phys. Rev. B **108**, 041406 (2023)
- [63] Winter, S.M., Li, Y., Jeschke, H.O., Valentí, R.: Challenges in design of Kitaev materials: Magnetic interactions from competing energy scales. Phys. Rev. B **93**, 214431 (2016)
- [64] Toth, S., Lake, B.: Linear spin wave theory for single-Q incommensurate magnetic

- structures. *J. Phys. Condens. Matter.* **27**, 166002 (2015)
- [65] Badrtdinov, D.I., Ding, L., Ritter, C., Hembacher, J., Ahmed, N., Skourski, Y., Tsirlin, A.A.: $\text{MoP}_3\text{SiO}_{11}$ honeycomb antiferromagnet with disconnected octahedra. *Phys. Rev. B* **104**, 094428 (2021)
- [66] Elbouaanani, L.K., Malaman, B., Gérardin, R.: Synthesis, crystal structure, and magnetic properties of $\text{FeP}_3\text{SiO}_{11}$: First example of iron(III)silicophosphate. *J. Solid. State Chem.* **147**, 565–572 (1999)
- [67] Koepnik, K., Eschrig, H.: Full-potential nonorthogonal local-orbital minimum-basis band-structure scheme. *Phys. Rev. B* **59**, 1743–1757 (1999)
- [68] Kresse, G., Furthmüller, J.: Efficiency of ab-initio total energy calculations for metals and semiconductors using a plane-wave basis set. *Computational Materials Science* **6**, 15–50 (1996)
- [69] Kresse, G., Furthmüller, J.: Efficient iterative schemes for ab initio total-energy calculations using a plane-wave basis set. *Phys. Rev. B* **54**, 11169–11186 (1996)
- [70] Perdew, J.P., Burke, K., Ernzerhof, M.: Generalized gradient approximation made simple. *Phys. Rev. Lett.* **77**, 3865–3868 (1996)
- [71] Zhang, H., McGuire, M.A., May, A.F., Chao, H.-Y., Zheng, Q., Chi, M., Sales, B.C., Mandrus, D.G., Nagler, S.E., Miao, H., Ye, F., Yan, J.: Stacking disorder and thermal transport properties of $\alpha\text{-RuCl}_3$. *Phys. Rev. Mater.* **8**, 014402 (2024)
- [72] Bertinshaw, J., Kim, Y.K., Khaliullin, G., Kim, B.J.: Square lattice iridates. *Ann. Rev. Condens. Matter Phys.* **10**, 315–336 (2019)
- [73] Rau, J.G., Lee, E.K.-H., Kee, H.-Y.: Generic spin model for the honeycomb iridates beyond the Kitaev limit. *Phys. Rev. Lett.* **112**, 077204 (2014)
- [74] Halloran, T., Desrochers, F., Zhang, E.Z., Chen, T., Chern, L.E., Xu, Z., Winn, B., Graves-Brook, M., Stone, M.B., Kolesnikov, A.I., Qiu, Y., Zhong, R., Cava, R., Kim, Y.B., Broholm, C.: Geometrical frustration versus Kitaev interactions in $\text{BaCo}_2(\text{AsO}_4)_2$. *Proc. Natl. Acad. Sci. U.S.A.* **120**, 2215509119 (2023)

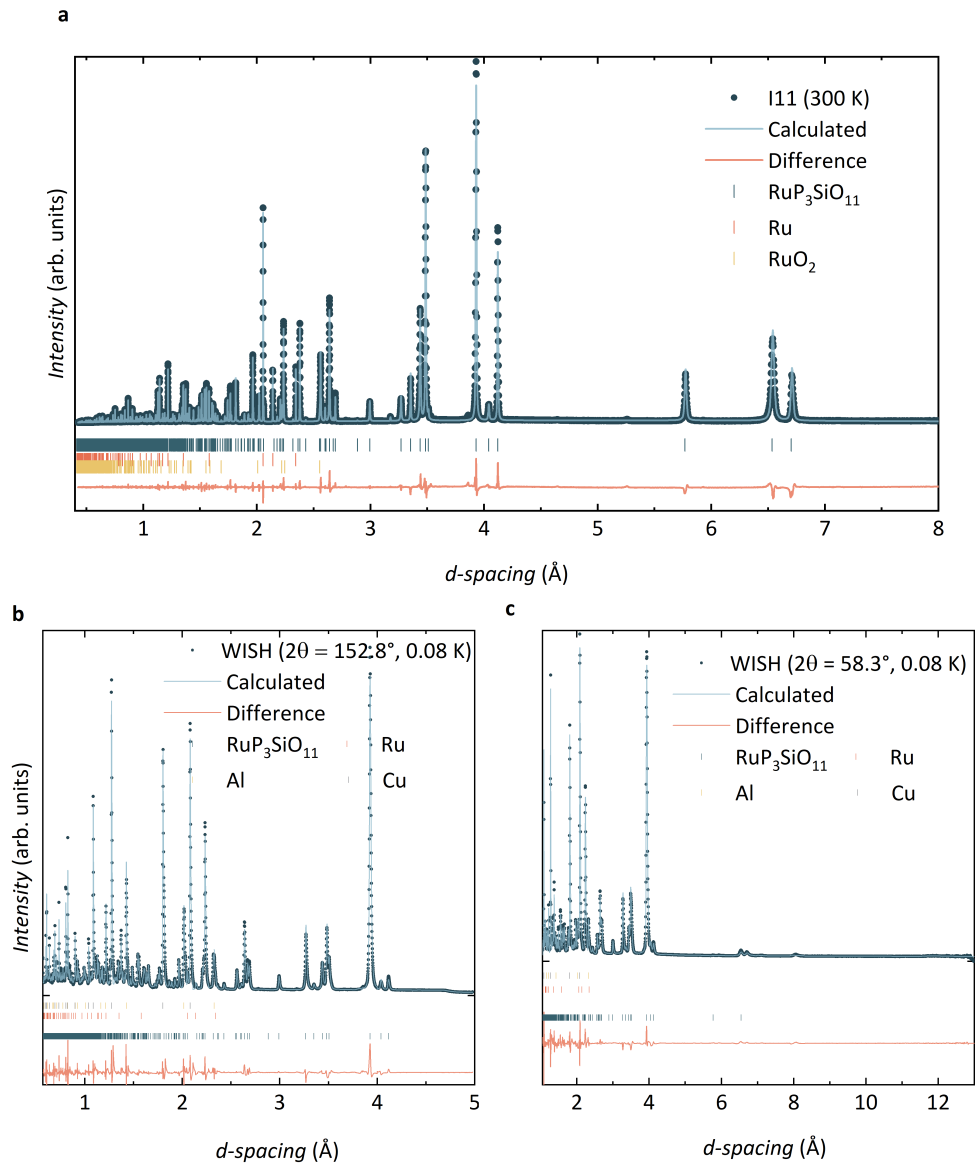


Fig. A1 **a** Rietveld analysis of powder X-ray diffraction data (300 K, I11, Diamond) using the $R\bar{3}m$ structural model that describes the crystal structure of $\text{RuP}_3\text{SiO}_{11}$. **b,c** Rietveld analysis of powder neutron diffraction data (WISH, ISIS) confirming that $\text{RuP}_3\text{SiO}_{11}$ maintains the $R\bar{3}c$ structural model down to a base temperature of 0.08 K.

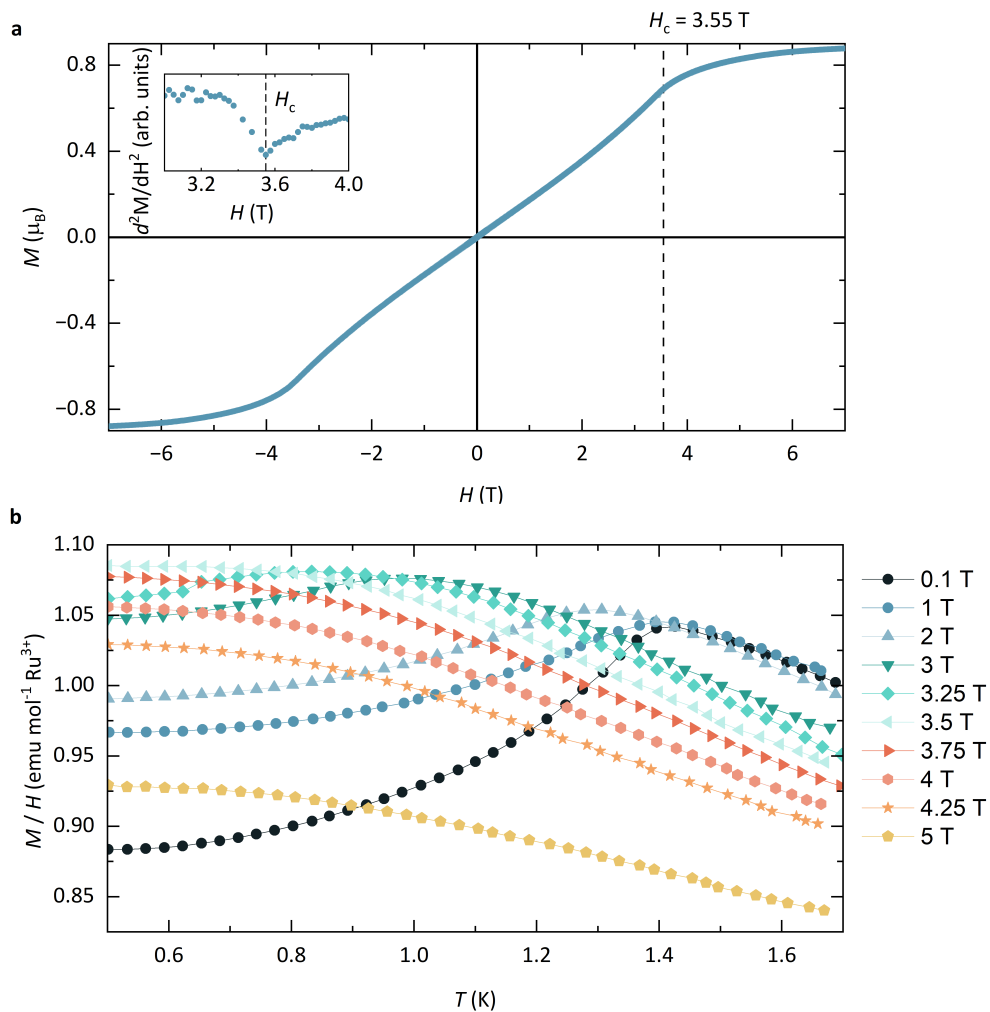


Fig. A2 **a** The magnetisation isotherm of RPSO measured at 0.4 K increases linearly with the applied field up to 2 T, beyond which the rate of increase in magnetisation becomes steeper before reaching a critical field, $H_C = 3.55$ T. **a, inset** The second field derivative of the magnetisation highlighting $H_C = 3.55$ T. **b** The effect of this critical field can be observed in the field dependence of M/H , where the ordering temperature is suppressed above H_C .

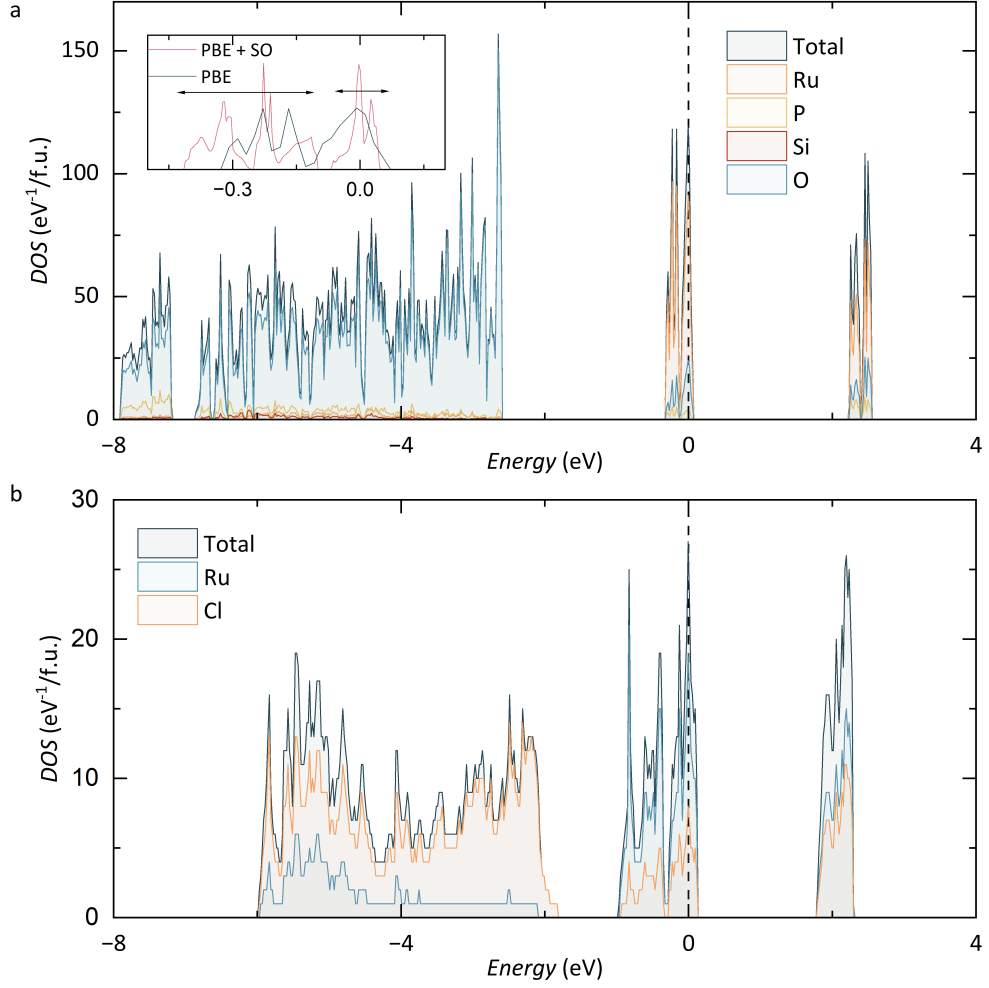


Fig. A3 PBE density of states for **a** RPSO and **b** α -RuCl₃ (bottom). The Fermi level (E_f) is at zero energy. The inset shows a comparison of PBE and PBE+SO density of states around E_f , with the arrows labeling the regions of $j_{\text{eff}} = \frac{3}{2}$ and $\frac{1}{2}$ states.

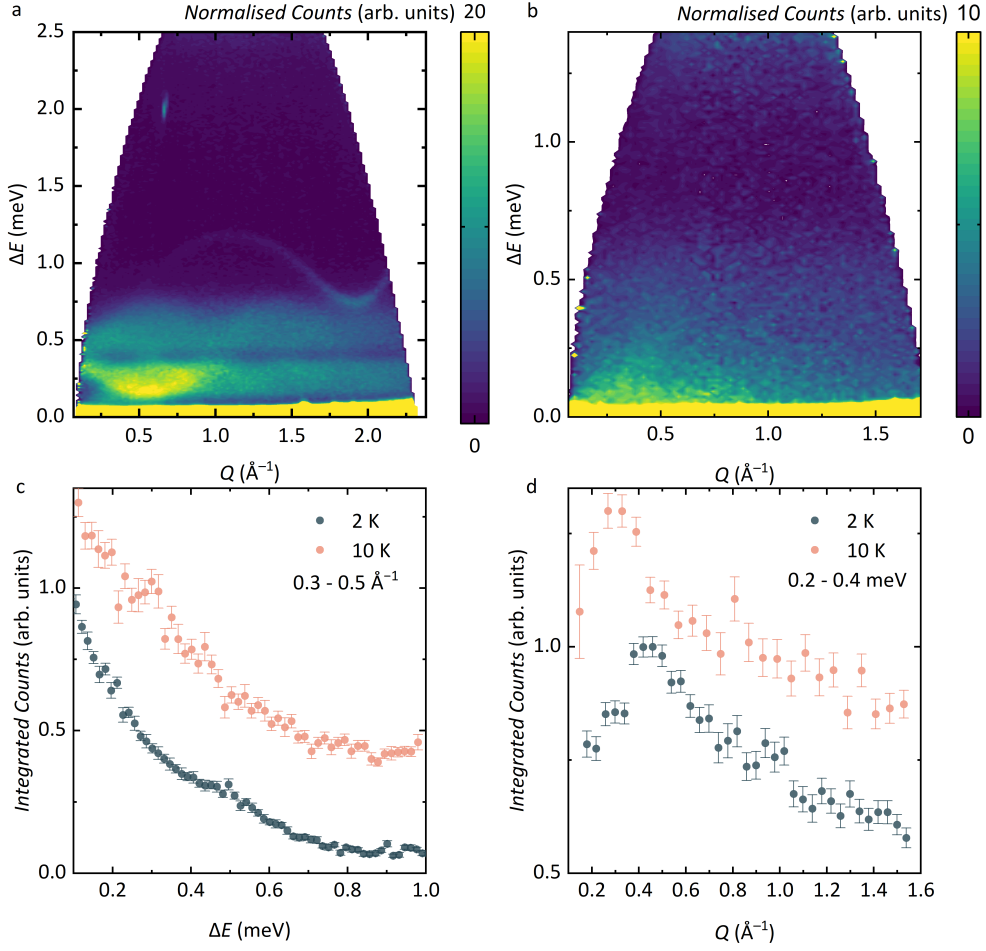


Fig. A4 **a** The experimental dynamical structure factor, $S(Q, \Delta E = \hbar\omega)_{\text{exp}}$ of RPSO measured at 0.08 K and $E_i = 3.14$ meV (LET, ISIS) shows a clear excitation gap of approximately 0.1 meV and two branches of magnetic excitations extending up to 0.8 meV. **b** Above T_N at 2 K, the excitation gap closes, and **c-d** ΔE - and $|Q|$ -integrated cuts show that structured magnetic scattering remains up to 10 K.

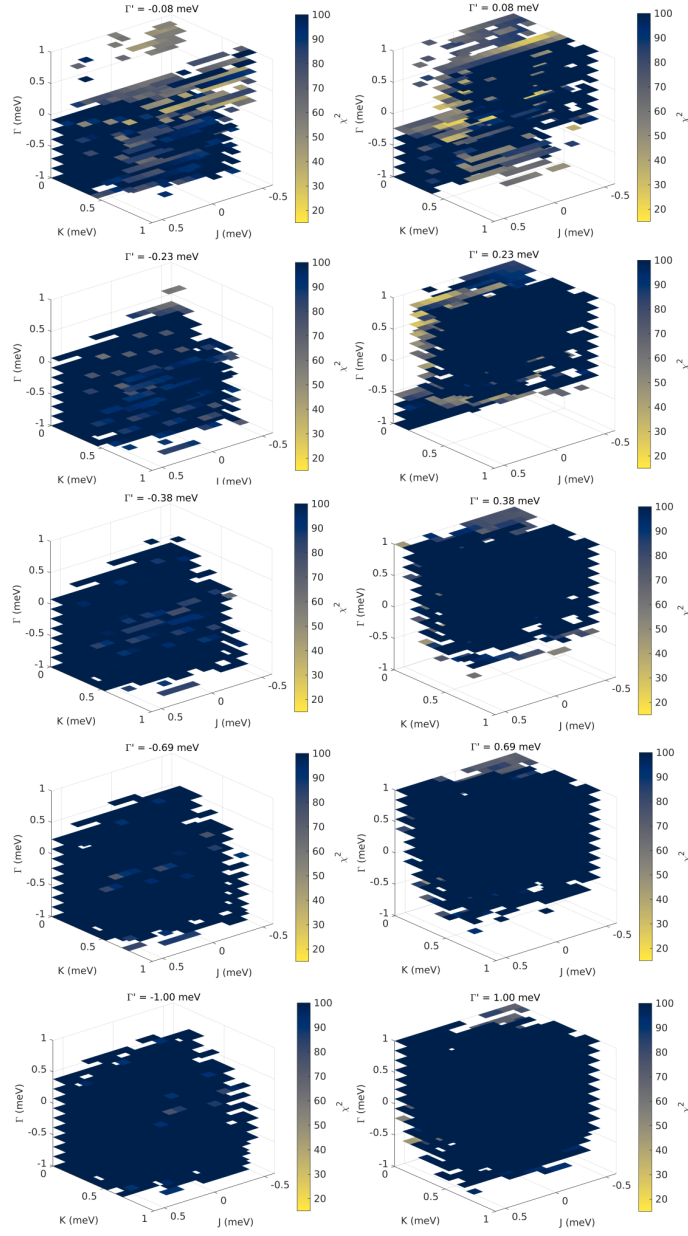


Fig. A5 Fit quality, represented by χ^2 , for the $\mathcal{H}_{JK\Gamma'}$ model fitted to 8 ΔE cuts with $K > 0$. Each four-dimensional space illustrates the variation of $-0.6 < J < 0.6$ meV, $0 < K < 1$ meV, and $-1 < \Gamma < 1$ meV, in 14 linearly spaced steps for a specific Γ' value, with the intensity reflecting the corresponding χ^2 values. Missing regions represent solutions that are incompatible with the Néel ordered ground state.

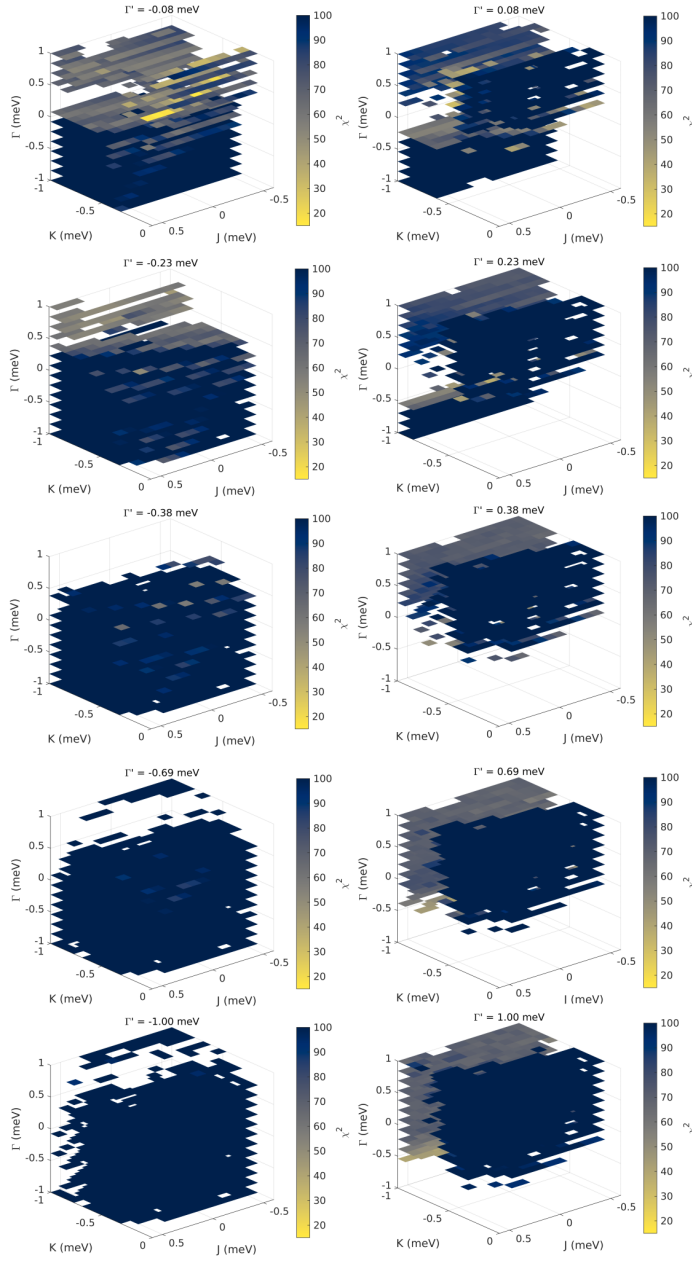


Fig. A6 Fit quality, represented by χ^2 , for the $\mathcal{H}_{JK\Gamma\Gamma'}$ model fitted to 8 ΔE cuts with $K < 0$. Each four-dimensional space illustrates the variation of $-0.6 < J < 0.6$ meV, $-1 < K < 0$ meV, and $-1 < \Gamma < 1$ meV, in 14 linearly spaced steps for a specific Γ' value, with the intensity reflecting the corresponding χ^2 values. Missing regions represent solutions that are incompatible with the Néel ordered ground state.

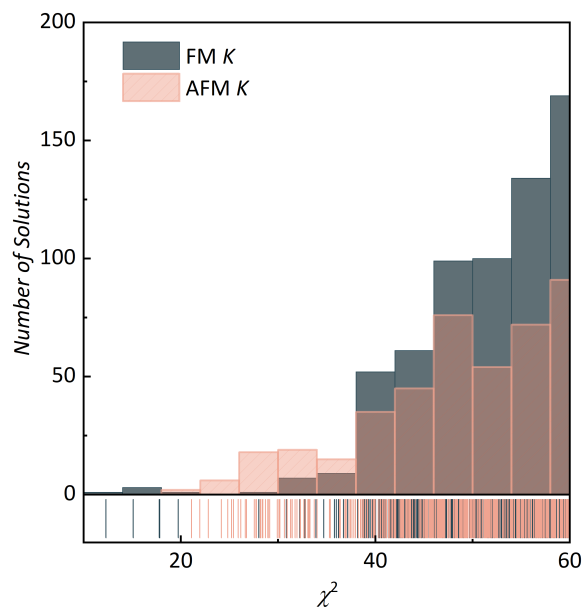


Fig. A7 The number solutions as a function of χ^2 for the parameter sets obtained in the $\mathcal{H}_{JKT\Gamma'}$ grid search for $K > 0$ and $K < 0$.